

IMS³: Breaking Distributional Aggregation in Diffusion-Based Dataset Distillation

Chenru Wang^{1*} Yunyi Chen^{1,2*} Zijun Yang³ Joey Tianyi Zhou^{4,5} Chi Zhang^{1†}
¹AGI Lab, Westlake University, ²Eindhoven University of Technology,
³Jinan University, ⁴IHPC, Agency for Science, Technology and Research, Singapore
⁵CFAR, Agency for Science, Technology and Research, Singapore

Abstract

Dataset Distillation aims to synthesize compact datasets that can approximate the training efficacy of large-scale real datasets, offering an efficient solution to the increasing computational demands of modern deep learning. Recently, diffusion-based dataset distillation methods have shown great promise by leveraging the strong generative capacity of diffusion models to produce diverse and structurally consistent samples. However, a fundamental goal misalignment persists: diffusion models are optimized for generative likelihood rather than discriminative utility, resulting in over-concentration in high-density regions and inadequate coverage of boundary samples crucial for classification. To address this issue, we propose two complementary strategies. Inversion-Matching (IM) introduces an inversion-guided fine-tuning process that aligns denoising trajectories with their inversion counterparts, broadening distributional coverage and enhancing diversity. Selective Subgroup Sampling (S^3) is a training-free sampling mechanism that improves inter-class separability by selecting synthetic subsets that are both representative and distinctive. Extensive experiments demonstrate that our approach significantly enhances the discriminative quality and generalization of distilled datasets, achieving state-of-the-art performance among diffusion-based methods.

1 Introduction

The rapid growth of deep learning has been accompanied by an equally rapid increase in dataset size and computational demands [16, 25]. To reduce training costs and memory requirements, researchers have explored dataset reduction strategies. Early approaches often relied on data pruning, which selects a subset of the original data but suffers from a limited compression ratio. Recently, Dataset Dis-

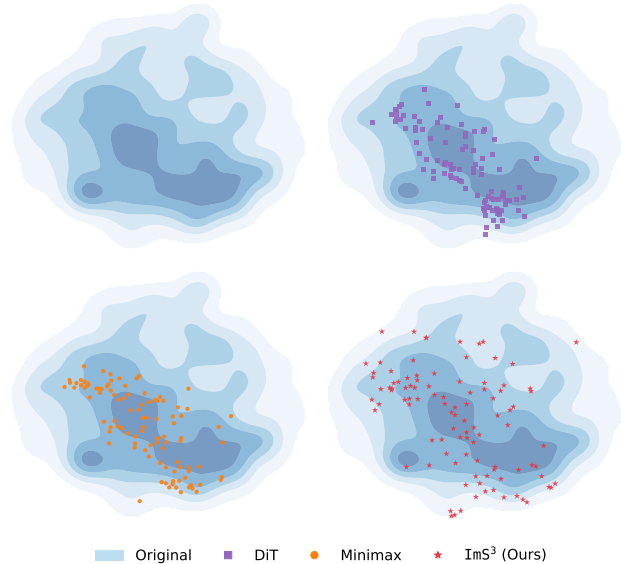


Figure 1. t-SNE visualization of feature distributions for different distilled datasets. The blue density map represents the feature distribution of the original dataset. The purple squares correspond to samples generated by the DiT [23], the orange dots correspond to Minimax [8], and the red stars indicate samples produced by our ImS³. Our method covers a broader area of the feature space, indicating improved distributional coverage.

tillation has emerged as a more effective paradigm [2, 7, 26, 27, 39, 40, 48, 49, 52]. Instead of directly selecting from the original dataset, distillation generates a compact synthetic dataset that can approximate the training performance of the full dataset. This generative perspective enables substantially higher compression ratios while maintaining competitive accuracy, making dataset distillation an attractive solution in modern large-scale learning scenarios.

Earlier works mainly formulated dataset distillation as an optimization problem, where a small set of synthetic samples is directly optimized to match the statistical or gradient information of the original dataset [2, 6, 14, 17,

*These authors contributed equally.

†Corresponding author.

22, 49]. However, such optimization-based methods often suffer from high computational costs and poor scalability to high-resolution or large-class datasets due to their reliance on iterative gradient alignment and sample-specific updates. Recently, with the emergence and widespread adoption of diffusion models [9, 30, 31, 36], diffusion-based dataset distillation methods have emerged and been widely adopted [3, 4, 8, 21, 32, 37, 42, 50, 53]. By leveraging the generative capacity of diffusion models, diffusion-based methods benefit from their probabilistic formulation, which allows them to capture complex data manifolds and generate samples with higher stability and structural consistency [15], these methods can synthesize high-quality and diverse samples while preserving the underlying structure of the original dataset. Typically, diffusion-based distillation consists of two stages, fine-tuning and sampling, which respectively adapt the generative model and determine how distilled samples are drawn. Compared with optimization-based methods, diffusion-based distillation offers improved fidelity, scalability, and robustness, making it a promising direction for large-scale applications.

Despite these advances, existing diffusion-based dataset distillation methods face a fundamental goal misalignment between generation and discrimination. A diffusion model is inherently generative, trained to maximize data likelihood and thereby concentrate on high-density regions of the data manifold [1, 9, 13]. In contrast, dataset distillation serves a discriminative objective, where effective dataset distillation requires capturing critical samples near decision boundaries that are often low-density and hard to learn. This mismatch leads to what we refer to as distributional aggregation, where synthetic data are overly concentrated in high-density areas while underrepresenting boundary regions crucial for generalization and robust discrimination. As illustrated in Fig. 1, diffusion-based methods such as Minimax [8] exhibit a strong aggregation of samples in high-density regions of the feature space, whereas our proposed ImS^3 produces more uniformly distributed features, indicating improved coverage and representation diversity.

To address this issue, we aim to mitigate the model’s inherent high-density bias and improve the representational diversity of synthetic datasets. To achieve this goal, we exploit a distinctive property of the diffusion inversion process: its inherent instability causes inversion trajectories to deviate from high-density regions and naturally shift toward low-density areas of the data manifold [20, 46]. Building upon this insight, we propose Inversion-Matching (IM), a novel fine-tuning strategy, which explicitly aligns the noise latent with its inversion counterpart at corresponding timestep. This alignment serves as a corrective signal that encourages the model to broaden its distributional coverage, fill underrepresented regions, and enhance sample diversity, thereby producing more discriminative and representative

distilled datasets.

Standard diffusion sampling procedures are primarily designed for generative quality rather than discriminative utility [18, 19, 30]. They typically generate data for each class independently, without explicitly considering inter-class relationships. As a result, the synthesized samples, though visually plausible, may lead to reduced discriminative power in downstream classifiers. To explicitly enhance the class separability of distilled datasets, we propose Selective Subgroup Sampling (S^3), a training-free inference-time sampling strategy tailored to improve discriminative representation. Specifically, during the generation of each class, S^3 produces multiple candidate sample groups in the feature space and evaluates them based on two complementary criteria: proximity to the real data centroid (ensuring representativeness) and separation from other class centroids (ensuring distinction). The candidate group that best satisfies both criteria is selected as the distilled subset. This simple yet effective mechanism introduces class awareness into the sampling process without any additional training cost. By encouraging each class’s synthetic samples to be both representative and well-separated, S^3 enhances the inter-class discrimination of the distilled dataset and significantly improves the downstream classification performance.

In summary, we revisit the key challenges of dataset distillation and address them from two complementary perspectives. IM expands the coverage of synthetic data by guiding the diffusion model toward low-density regions, thereby mitigating distributional aggregation and improving representation diversity. S^3 further enhances the discriminative structure of the distilled dataset by explicitly promoting inter-class separation during sampling. To validate the effectiveness of our strategy, we conduct extensive experiments across multiple datasets and model architectures. The results demonstrate that our method consistently achieves superior accuracy compared with existing diffusion-based distillation approaches, confirming the effectiveness of the proposed fine-tuning and sampling strategies.

Our contributions are summarized as follows:

- We propose IM to mitigate distributional aggregation and improve coverage of low-density regions.
- We introduce S^3 , a training-free sampling strategy that enhances inter-class discriminability.
- Extensive experiments demonstrate that our approach achieves state-of-the-art performance on multiple datasets. Code and model will be publicly released to facilitate future research.

2 Related Works

2.1 Non-generative Dataset Distillation

Early studies on dataset distillation mainly adopt optimization-based paradigms, where a compact syn-

thetic set is directly optimized to approximate the training dynamics of real data. The seminal work Dataset Distillation [40] formulates this task as a bi-level optimization problem that minimizes the gradient mismatch between real and synthetic batches. To improve efficiency and scalability, SRe²L [45] and its following works [29, 44, 51] adopt a uni-level optimization framework that learns shared representations and relaxed labels, significantly reducing computation while maintaining performance. Other representative approaches, such as Matching Training Trajectories (MTT) [2] and Gradient Matching [49], further improve gradient alignment or optimize learning trajectories. Although these methods achieve promising results on small-scale datasets, they generally struggle to scale to high-resolution or large-class scenarios due to the inherent optimization burden and limited generative diversity.

2.2 Diffusion-based Dataset Distillation

Recent studies have leveraged diffusion models for dataset distillation to synthesize compact yet representative datasets. A representative work, Minimax Diffusion [8], fully utilizes pre-trained diffusion models for generating realistic synthetic datasets and fine-tunes them with a min-max criterion to enhance both sample representativeness and diversity. Following this line, D⁴M [32] adopts pre-trained text-to-image diffusion models and integrates prototype learning to cluster latent features and learn category centers, thereby improving intra-class consistency and visual fidelity. To address distribution mismatch and randomness in latent sampling, D³HR [50] introduces a domain-mapping framework that employs DDIM inversion to map VAE latents into a Gaussian domain with higher normality, coupled with a group-sampling strategy for improved representativeness and distribution alignment. More recently, DDVLC [53] extends diffusion-based distillation into the vision–language domain by constructing paired image-text prototypes via large language models, effectively enhancing semantic coherence and mitigating illogical or missing-object artifacts during generation. While these methods markedly improve fidelity and scalability over optimization-based approaches, they still exhibit distributional aggregation, where generated samples tend to cluster in high-density regions, reducing diversity and coverage of fine-grained low-density patterns.

2.3 Inversion in Diffusion Models

In diffusion models, inversion aims to trace a real image back to its originating noise. While the reverse process can directly add noise and reach the initial noise state in a single reverse step, inversion must recover the latent trajectory through step-by-step estimation of the intermediate states. This technique has been widely used in

diffusion-based editing, alignment, watermark, and reconstruction [5, 12, 20, 24, 30, 38], providing a means to bridge real and generative data domains.

However, recent studies have shown that inversion process has inherent instability due to the compounding approximation error along the inversion trajectory [46]. Since the forward and inverse dynamics are not perfectly symmetric, small local errors can accumulate and push the inversion path away from high-density manifolds of the real data distribution. Consequently, inverted latents often drift toward low-density regions of the data space, forming an implicit bias that reflects structural inconsistencies between the true and modeled distributions. While this instability is generally undesirable in reconstruction tasks, our work leverages it as a beneficial property to intentionally expand the coverage of low-density areas during fine-tuning, thereby mitigating the over-aggregation problem in diffusion models.

3 Preliminary

Before introducing our methodology, we first provide some necessary background information in this section.

3.1 Dataset Distillation

Dataset distillation aims to construct a compact synthetic dataset that can approximate the training efficacy of the original large-scale dataset. Given an original dataset $\mathcal{D}_r = \{(x_i, y_i)\}_{i=1}^N$ with C_{cls} classes, the goal is to synthesize a much smaller distilled dataset $\mathcal{D}_s = \{(\tilde{x}_j, \tilde{y}_j)\}_{j=1}^M$, where $M \ll N$. A model trained on \mathcal{D}_s should achieve comparable or even higher performance to one trained on \mathcal{D}_r when evaluated on unseen real data.

In practice, the effectiveness of dataset distillation is typically measured under the *Images Per Class* (IPC) setting, where each class in \mathcal{D}_s contains a limited number of samples (*e.g.*, 1, 10, or 50). The central challenge lies in generating or selecting these few samples such that they preserve both the coverage and the discriminative structure of the original distribution, enabling models trained on the distilled data to generalize effectively.

3.2 DDIM Inversion

Consider a deterministic DDIM sampler with $\eta = 0$ and cumulative noise schedule $\bar{\alpha}_t \in (0, 1]$. The forward denoising update can be written as

$$\mathbf{z}_{t-1} = \sqrt{\bar{\alpha}_{t-1}} \hat{\mathbf{z}}_0(\mathbf{z}_t, t) + \sqrt{1 - \bar{\alpha}_{t-1}} \varepsilon_\theta(\mathbf{z}_t, t), \quad (1)$$

where

$$\hat{\mathbf{z}}_0(\mathbf{z}_t, t) = \frac{\mathbf{z}_t - \sqrt{1 - \bar{\alpha}_t} \varepsilon_\theta(\mathbf{z}_t, t)}{\sqrt{\bar{\alpha}_t}}. \quad (2)$$

DDIM inversion (Euler scheduler) performs the reverse of the sampling process, mapping a real image into its latent

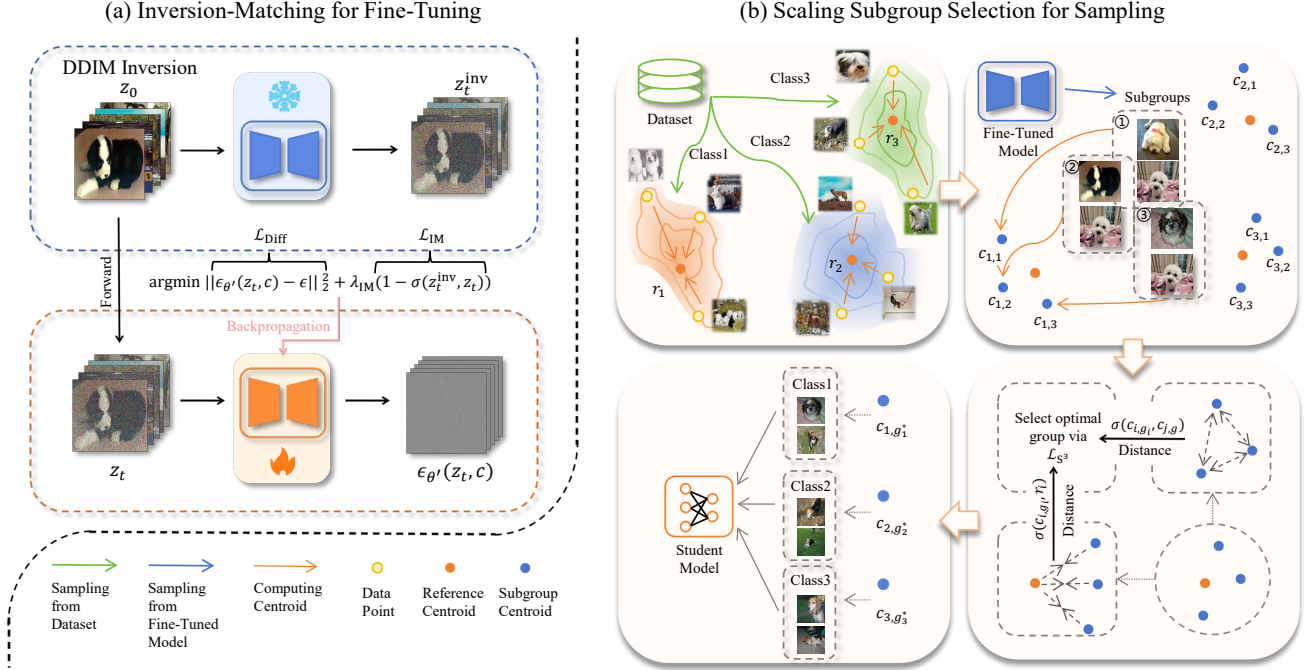


Figure 2. Overview of the proposed ImS^3 framework. (a) IM fine-tuning expands distribution coverage by aligning denoised and inverted latents through the IM loss \mathcal{L}_{IM} . (b) S^3 enhances discriminative diversity during sampling by selecting representative subgroups whose centroids are close to real data centroids while maintaining inter-class separation, optimized via \mathcal{L}_{S^3} . r_i denotes the centroid of real samples from the i -th class, while c_{i,g_i} represents the centroid of the g_i -th candidate subgroup synthesized by the diffusion model for the same class. The selected optimal subgroup centroid c_{i,g_i}^* strikes the best balance between representativeness to the real class distribution and distinctiveness from other classes.

noise. Based on the DDIM update rule, the inversion step of Euler scheduler using approximation is given by:

$$\mathbf{z}_{t_i} = \mathbf{z}_{t_{i-1}} + (\sigma_{t_i} - \sigma_{t_{i-1}})\varepsilon_{\theta}(\mathbf{z}_{t_{i-1}}, t_{i-1}), \quad (3)$$

where σ_{t_i} and $\sigma_{t_{i-1}}$ are scheduling parameters.

Theoretically, reconstructions along inversion trajectories tend to occupy low-density regions of the data manifold due to the inherent instability of the inversion process [46], as discussed in Sec. 2. *In this work, we exploit this property during fine-tuning to intentionally guide the generative model toward underrepresented, low-density areas, which will be further elaborated in Sec. 4.1.* A more detailed introduction of the inversion instability is provided in the Appendix.

4 Method

In this section, we introduce our diffusion-based dataset distillation strategies, termed ImS^3 . The proposed method aims to construct a compact yet representative synthetic dataset by enhancing both distributional coverage and discriminative diversity. The overall pipeline of ImS^3 is illustrated in Fig. 2. It consists of two stages: Inversion-Matching (IM) fine-tunes a pre-trained diffusion model to

expand low-density coverage by aligning denoised and inverted latents, while Selective Subgroup Sampling (S^3) enhances discriminative diversity during sampling by selecting representative subgroups based on centroid similarity.

4.1 Inversion-Matching for Fine-Tuning

Diffusion-based dataset distillation typically involves fine-tuning a pre-trained generative model on the target dataset, followed by using the adapted model to synthesize a compact distilled dataset. However, this process often suffers from distributional aggregation, where generated samples concentrate in high-density regions of the data manifold, leaving low-density regions underrepresented, where decision boundaries usually lie and which are essential for effective dataset distillation.

To mitigate this imbalance, we develop IM, a fine-tuning strategy that leverages the intrinsic property of inversion, whose inherent instability causes the inversion trajectories to deviate from high-density regions, guiding the generative model toward broader coverage of the data space. Here, we choose the DiT-XL/2 [23] as the pre-trained diffusion model. This method can be decomposed into the following two parts.

Training Objective. To enable the model to learn a distribution with broader coverage, we first follow the deterministic DDIM inversion in Eq. (3) to compute the inversion noise latent $\mathbf{z}_t^{\text{inv}}$ at timestep t . For efficiency, instead of reconstructing the denoised latent by running the entire denoising trajectory from T to t , we directly sample the noise latent at timestep t by

$$\mathbf{z}_t = \sqrt{\bar{\alpha}_t} \mathbf{z}_0 + \sqrt{1 - \bar{\alpha}_t} \boldsymbol{\epsilon}, \quad (4)$$

where $\boldsymbol{\epsilon} \sim \mathcal{N}(0, \mathbf{I})$. We then perform time-aligned IM, that is, matching the noise latent and inverted noise latent at the same timestep t using

$$\mathcal{L}_{\text{IM}} = 1 - \sigma(\mathbf{z}_t^{\text{inv}}, \mathbf{z}_t), \quad (5)$$

where $\sigma(\cdot, \cdot)$ denotes cosine similarity. This objective aligns the noise latent \mathbf{z}_t with the inverted noise latent $\mathbf{z}_t^{\text{inv}}$ without enforcing exact equality between the two latent states, thereby guiding the model to capture underrepresented regions of the data manifold.

Additionally, in order to prevent the excessive distributional shift that can degrade the fidelity of generated images, we include the standard diffusion loss to minimize the squared error between the predicted noise $\epsilon_\theta(\mathbf{z}_t, c)$ and the ground truth $\boldsymbol{\epsilon}$:

$$\mathcal{L}_{\text{Diff}} = \|\epsilon_\theta(\mathbf{z}_t, c) - \boldsymbol{\epsilon}\|_2^2. \quad (6)$$

The overall fine-tuning loss combines high-density fidelity and low-density coverage:

$$\mathcal{L} = \mathcal{L}_{\text{Diff}} + \lambda_{\text{IM}} \mathcal{L}_{\text{IM}}, \quad (7)$$

where $\lambda_{\text{IM}} > 0$ balances the two terms (analysis see Appendix).

Full fine-tuning of \mathcal{G}_θ is computationally expensive and memory-intensive. Following Minimax Diffusion [8] and for efficiency, we adopt a Parameter Efficient Fine-Tuning (PEFT) approach via DiffFit [43], which inserts lightweight adapters into attention/MLP blocks and updates only these small modules while freezing the backbone, thereby reducing trainable parameters and compute without sacrificing stability or fidelity.

Algorithm 1 outlines the fine-tuning stage, where noise latent and inverted noise latent are aligned through a cosine-similarity loss. Combined with the standard diffusion loss. Overall, our fine-tuning strategy enables efficient adaptation of the diffusion model without introducing significant computational overhead, while effectively expanding distributional coverage and preserving generation fidelity.

4.2 Selective Subgroup Sampling

Standard diffusion sampling primarily focuses on generative fidelity, often ignoring inter-class relationships among

Algorithm 1: Inversion-Matching (IM)

Input: Pre-trained parameters θ , encoder E , class encoder E_c , real dataset \mathcal{D}_r , feature extractor $\phi(\cdot)$

Output: Fine-tuned generator $\mathcal{G}_{\theta'}$

Initialize: $\theta' \leftarrow \theta$

- 1 **for** each real sample $(x_0, y_0) \sim \mathcal{D}_r$ **do**
 - 2 Sample timestep t and noise $\boldsymbol{\epsilon} \sim \mathcal{N}(0, \mathbf{I})$;
 - 3 Compute latent $z_0 \leftarrow E(x_0)$ and class embedding $c \leftarrow E_c(y_0)$;
 - 4 Obtain inversion state
 $z_t^{\text{inv}} \leftarrow \text{Inversion}(z_0, t, \theta')$ Compute noisy latent: $z_t \leftarrow \sqrt{\bar{\alpha}_t} z_0 + \sqrt{1 - \bar{\alpha}_t} \boldsymbol{\epsilon}$;
 - 5 Compute diffusion loss:
 $\mathcal{L}_{\text{Diff}} = \|\epsilon_{\theta'}(z_t, c) - \boldsymbol{\epsilon}\|_2^2$;
 - 6 Compute inversion-matching loss:
 $\mathcal{L}_{\text{IM}} = 1 - \sigma(z_t^{\text{inv}}, z_t)$;
 - 7 Update the model parameter θ' with Eq. (7);
 - 8 **end**
 - 9 Set $\mathcal{G}_{\theta'}$ as the fine-tuned generator;
-

categories. As a result, the synthesized data may lack sufficient discriminative structure, which is critical for effective dataset distillation.

To address this issue, we propose \mathcal{S}^3 , a training-free sampling strategy that aims to ensure the distilled samples in each class are close to the real samples of the same class while remaining far from the distilled samples of other classes. To achieve this, \mathcal{S}^3 selects representative and diverse subgroups based on centroid similarity.

Reference Centroids. To measure and align the differences between real and synthetic distributions, thereby achieving our goal of balancing coverage and discrimination, we employ a cluster centroid representation to quantify distributional relations.

Formally, let \mathcal{D}_r be a labeled dataset with C classes in the distilled setting. A frozen feature encoder $\phi : \mathbb{R}^{H \times W \times 3} \rightarrow \mathbb{S}^{C_{\text{Channel}}}$ maps images to ℓ_2 -normalized embeddings on the unit sphere. For class i , denote the real subset with K_i samples by \mathcal{D}_i (analysis see Sec. 5.3), and define the real class centroid

$$r_i = \left\| \frac{1}{K_i} \sum_{x \in \mathcal{D}_i} \phi(x) \right\|_2 \in \mathbb{S}^{C_{\text{Channel}}}. \quad (8)$$

Candidate Subgroups and Centroids. Following the definition aforementioned, we compute the centroids of the subgroups. Suppose that $\mathcal{C} = \{1, 2, \dots, C\}$ and $\mathcal{G} = \{1, 2, \dots, G\}$. For each class $i \in \mathcal{C}$, we draw G candidate subgroups $\{\mathcal{S}_{i, g_i}\}_{g_i \in \mathcal{G}}$ from a pretrained diffusion generator \mathcal{G}_θ (e.g., DiT [23]) and a frozen VAE decoder (analysis

Algorithm 2: Selective Subgroup Sampling (S^3)

Input: Fine-tuned generator $\mathcal{G}_{\theta'}$, real dataset $\mathcal{D}_r = \{\mathcal{D}_i\}_{i=1}^C$, feature extractor $\phi(\cdot)$, number of candidates G

Output: Distilled dataset $\mathcal{D}_s = \{S_i^*\}_{i=1}^C$

Initialize: Randomly initialize

$$\mathbf{g}^{(0)} = (g_1^{(0)}, \dots, g_C^{(0)}), \text{ where } g_i^{(0)} \in \mathcal{G}$$

```
1 for each class  $i \in \mathcal{C}$  do
2   Compute reference centroid:
    $r_i \leftarrow \left\| \frac{1}{K_i} \sum_{x \in \mathcal{D}_i} \phi(x) \right\|_2$ ;
3   Generate  $G$  subgroups  $S_{i,g_i}$  with  $K$  samples
   using  $\mathcal{G}_{\theta'}$ ;
4   for  $g_i = 1$  to  $G$  do
5     Compute subgroup centroid:
      $c_{i,g_i} \leftarrow \left\| \frac{1}{K} \sum_{x \in S_{i,g_i}} \phi(x) \right\|_2$ ;
6   end
7 end

8 Initialize  $\mathbf{g} \leftarrow \mathbf{g}^{(0)}$ ;
9 while not converged do
10  | Update  $\mathbf{g}$  to reduce  $\mathcal{L}_{S^3}(\mathbf{g})$  via Eq. (10)
11 end
12 Set  $S_i^* \leftarrow S_{i,g_i^*}$  for all  $i \in \mathcal{C}$  using
    $\mathbf{g}^* = \arg \min_{\mathbf{g}} \mathcal{L}_{S^3}(\mathbf{g})$ ;
13 return  $\mathcal{D}_s = \{S_i^*\}_{i=1}^C$ ;
```

of G see Appendix); each subgroup contains K images. All candidate images are embedded by ϕ , and each subgroup centroid is defined as

$$c_{i,g_i} = \left\| \frac{1}{K} \sum_{x \in S_{i,g_i}} \phi(x) \right\|_2 \in \mathbb{S}^{C_{\text{Channel}}}. \quad (9)$$

After obtaining all subgroup centroids, we evaluate them based on their representativeness and discriminative separation to identify the optimal subset for each class.

Selection Objective. We select one subgroup per class by minimizing a objective that balances proximity to real centroids and inter-class separation:

$$\begin{aligned} \mathcal{L}_{S^3}(\mathbf{g}) = & \alpha \sum_{i=1}^C \log(1 - \sigma(c_{i,g_i}, r_i)) \\ & - \frac{\beta}{(C-1)G} \sum_{i=1}^C \sum_{\substack{j=1 \\ j \neq i}}^C \sum_{g=1}^G \log(1 - \sigma(c_{i,g_i}, c_{j,g})), \end{aligned} \quad (10)$$

where $\alpha, \beta > 0$ weight the two criteria (analysis see Sec. 5.3), and $\mathbf{g} = (g_1, \dots, g_C)$ is a vector of subgroup

indices, with $g_i \in \mathcal{G}$ indicating the selected subgroup for class i . The first term contracts subgroup centroids toward their real counterparts, constraining synthetic data within the true distribution; the second term enlarges pairwise angles between subgroup centroids, preserving diversity and mitigating mode collapse.

Because Eq. (10) depends only on precomputed centroids, we obtain the optimal subset of indices via

$$\mathbf{g}^* = \arg \min_{\mathbf{g}} \mathcal{L}_{S^3}(\mathbf{g}), \quad (11)$$

where $\mathbf{g}^* = \{(i, g_i^*)\}_{i=1}^C$ denotes the indices of the optimal subgroup indices. Eq. (11) is solved using a simple greedy search strategy. These indices are then used to find the corresponding subgroups and construct the distilled dataset \mathcal{D}_s .

Algorithm 2 describes the sampling stage, which selects one representative subgroup per class by balancing proximity to real centroids and separation from other classes. Overall, this sampling strategy efficiently enhances the discriminative structure of the distilled dataset while preserving its representativeness and diversity.

5 Experiments

5.1 Experimental Settings

Datasets. We evaluate our method on high-resolution benchmarks to assess its scalability and generalization. Experiments are conducted on ImageNet [25] and its subsets, including ImageNette [10], ImageWoof [11], and ImageIDC[14] with 256×256 resolution, as well as ImageNet-100 [35]. ImageNette consists of 10 categories each, with ImageWoof containing 10 fine-grained dog breeds that exhibit high inter-class similarity, making it a challenging benchmark.

Implementation Details. We apply DiffFit [43] for parameter-efficient fine-tuning on a pretrained DiT-XL/2 [23]. All experiments in Sec. 5.2 are under different *Images Per Class* (IPC) settings. For ImageWoof, we evaluate all IPC levels of 10, 20, 50, 70, and 100. For ImageNette, we report results under IPC of 10, 20, and 50. For ImageIDC, we conduct experiments with IPC of 1, 10, and 50. The balancing coefficient λ_{IM} in Eq. (7) is set to 0.002. Both fine-tuning and sample generation are conducted at an image resolution of 256×256 . The diffusion model is fine-tuned for 8 epochs with a mini-batch size of 8 using AdamW with a learning rate of 1×10^{-3} . During the S^3 , the subgroup number G and the coefficients α and β are selected per dataset. We also examine the effect of K_i , the number of real samples used to compute each reference centroid. Representative findings on ImageWoof are reported in Sec. 5.3.

All experiments are performed on a single NVIDIA A100 GPU with 40GB of memory. Additional implementa-

Table 1. Comparison of SOTA dataset distillation methods on ImageWoof under various IPC and backbone settings. The best results are marked as bold, and the second are underlined.

IPC (Ratio)	Model	Random	K-Center [28]	Herding [41]	DiT [23]	Minimax [8]	DM [47]	IDC-1 [14]	D ⁴ M [32]	D ³ HR [50]	DDVLC [53]	ImS ³ (Ours)	Full
10 (0.8%)	ConvNet-6	24.3±1.1	19.4±0.9	26.7±0.5	34.2±1.1	34.1±0.4	26.9±1.2	33.3±1.1	29.4±0.9	–	<u>34.8±2.4</u>	35.6±1.8	86.4±0.2
	ResNetAP-10	29.4±0.8	22.1±0.1	32.0±0.3	34.7±0.5	35.7±0.3	30.3±1.2	39.1±0.5	33.2±2.1	<u>40.7±1.0</u>	39.5±1.5	41.8±0.3	87.5±0.5
	ResNet-18	27.7±0.9	21.1±0.4	30.2±1.2	34.7±0.4	37.6±0.9	33.4±0.7	37.3±0.2	32.3±1.2	39.6±1.0	<u>39.9±2.6</u>	41.3±1.1	89.3±1.2
20 (1.6%)	ConvNet-6	29.1±0.7	21.5±0.8	29.5±0.3	36.1±0.8	37.9±0.2	29.9±1.0	35.5±0.8	34.0±2.3	–	<u>37.9±1.9</u>	39.4±0.5	86.4±0.2
	ResNetAP-10	32.7±0.4	25.1±0.7	34.9±0.1	41.1±0.8	43.3±0.3	35.2±0.6	43.4±0.3	40.1±1.6	–	<u>44.5±2.2</u>	45.8±1.2	87.5±0.5
	ResNet-18	29.7±0.5	23.6±0.3	32.2±0.6	40.5±0.5	40.9±0.6	29.8±1.7	38.6±0.2	38.4±1.1	–	<u>44.5±2.0</u>	44.9±1.6	89.3±1.2
50 (3.8%)	ConvNet-6	41.3±0.6	36.5±1.0	40.3±0.7	46.5±0.8	51.4±0.4	44.4±1.0	43.9±1.2	47.4±0.9	–	<u>54.5±0.6</u>	54.6±0.1	86.4±0.2
	ResNetAP-10	47.2±1.3	40.6±0.4	49.1±0.7	49.3±0.2	54.4±0.6	47.1±1.1	48.3±1.0	51.7±3.2	<u>59.3±0.4</u>	57.3±0.5	60.1±0.7	87.5±0.5
	ResNet-18	47.9±1.8	39.6±1.0	48.3±1.2	50.1±0.5	53.9±0.6	46.2±0.6	48.3±0.8	53.7±2.2	57.6±0.4	<u>58.9±1.5</u>	60.1±1.1	89.3±1.2
70 (5.4%)	ConvNet-6	46.3±0.6	38.6±0.7	46.2±0.6	50.1±1.2	51.8±0.6	47.5±0.8	48.9±0.7	50.5±0.4	–	<u>55.8±1.7</u>	56.0±0.3	86.4±0.2
	ResNetAP-10	50.8±0.6	45.9±1.5	53.4±1.4	54.3±0.9	56.5±0.5	51.7±0.8	52.8±1.8	54.7±1.6	–	<u>60.6±0.3</u>	61.0±0.3	87.5±0.5
	ResNet-18	52.1±1.0	44.6±1.1	49.7±0.8	51.5±1.0	52.7±0.4	51.9±0.8	51.1±1.7	56.3±1.8	–	<u>60.3±0.3</u>	61.1±0.7	89.3±1.2
100 (7.7%)	ConvNet-6	52.2±0.4	45.1±0.5	54.4±1.1	53.4±0.3	55.5±0.6	55.0±1.3	53.2±0.9	57.9±1.5	–	<u>62.7±1.4</u>	61.0±0.6	86.4±0.2
	ResNetAP-10	59.4±1.0	54.8±0.2	61.7±0.9	58.3±0.8	59.9±0.4	56.4±0.8	56.1±0.9	59.5±1.8	64.7±0.3	<u>65.7±0.5</u>	66.0±0.8	87.5±0.5
	ResNet-18	61.5±1.3	50.4±0.4	59.3±0.7	58.9±1.3	57.6±0.6	60.2±1.0	58.3±1.2	63.8±1.3	66.8±0.6	<u>68.3±0.4</u>	68.4±0.8	89.3±1.2

Table 2. Comparison on ImageNette under different IPC settings. All the results are obtained on ResNetAP-10. The best results are marked as bold and the second are underlined.

IPC	Random	DiT [23]	Minimax [8]	D ⁴ M [32]	ImS ³ (Ours)
10	54.2±1.6	59.1±0.7	58.6±0.4	60.9±1.7	62.9±1.2
20	63.5±0.5	64.8±1.2	<u>70.6±0.3</u>	66.3±1.3	71.6±0.7
50	76.1±1.1	73.3±0.9	<u>83.7±0.4</u>	77.7±1.1	84.2±1.0

Table 3. Comparison on ImageIDC under different IPC settings. All the results are obtained on ResNet-18. The best results are marked as bold, and the second are underlined.

IPC	Random	SRe ² L [45]	DiT [23]	RDED [33]	Minimax [14]	ImS ³ (Ours)
1	12.7±0.5	17.2±1.2	<u>26.7±1.4</u>	15.9±0.9	22.4±0.6	28.5±2.0
10	48.1±0.8	23.6±2.0	<u>54.1±0.4</u>	33.8±2.0	51.9±1.4	56.2±0.6
50	68.1±0.7	45.7±1.3	<u>76.4±0.3</u>	<u>78.3±0.9</u>	78.3±0.2	78.5±1.5

tion details and extended experimental results are provided in the Appendix.

Baseline and Evaluation Metrics. We compare our method with both optimization-based and diffusion-based dataset distillation baselines, including K-Center [28], Herding [41], DM [47], [14], SRe²L [45], RDED [33], Minimax [8], D⁴M [32], D³HR [50], and DDVLC [53]. Each distilled dataset is used to train classification models from scratch (*e.g.*, ConvNet-6, ResNetAP-10, and ResNet-18) for 300 epochs with SGD and cosine learning rate decay, following the evaluation protocol introduced in Minimax [8]. We report the mean and standard deviation of Top-1 Accuracy over three random seeds as the primary evaluation metric. Currently, there are two evaluation paradigms for assessing distilled datasets: one based on hard labels [8], where models are trained directly with one-hot supervision, and the other on soft labels [34], where knowledge distillation transfers teacher predictions as continuous targets. Following the settings in [37], we evaluate our method under both paradigms and report the higher accuracy between the

two for each experiment.

5.2 Comparison Experiments

In this section, we present comprehensive comparisons between our approach and multiple state-of-the-art dataset distillation methods across three benchmark datasets: ImageWoof, ImageNette, and ImageIDC. Additional experimental results, including extended quantitative studies, qualitative visualizations, and evaluations on ImageNet-100 and ImageNet-1K, are provided in the Appendix.

ImageWoof. We evaluate our method on the fine-grained ImageWoof dataset, which contains 10 dog breeds with high inter-class similarity. Tab. 1 presents the comparison with representative optimization-based methods (*e.g.*, SRe²L [45]) and diffusion-based approaches including Minimax [8], D⁴M [32], D³HR [50], and DDVLC [53]. The gains are especially pronounced under low IPC budgets. For example, at IPC = 10, ImS³ improves ResNetAP-10 accuracy from 35.7% achieved by Minimax [8] and 39.5% achieved by DDVLC [53] to 41.8%, corresponding to absolute improvements of 6.1% and 2.3% respectively. On ResNet-18, the accuracy increases from 37.6% with Minimax [8] and 39.9% with DDVLC [53] to 41.3%, yielding gains of 3.7% and 1.4%. These improvements indicate that IM expands the model’s coverage of low-density yet discriminative regions, while S³ enhances class separability by selecting well-aligned subgroups. As IPC increases, ImS³ consistently superior, demonstrating robust performance across different compression ratios and confirming that our method yields synthetic datasets that are both representative and discriminatively structured.

ImageNette. We evaluate our method on the high-resolution ImageNette dataset, which contains 10 natural object categories and provides a clean yet challenging benchmark for assessing the quality of distilled samples. Using the ResNetAP-10 backbone, the results in Tab. 2 show that our method consistently outperforms all

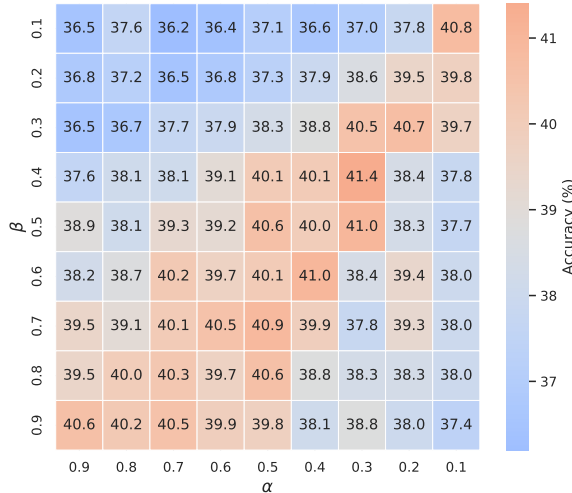


Figure 3. Heatmap of classification accuracy under different combinations of α and β . The heatmap shows that balanced values of α and β yield the best performance.

diffusion-based baselines. In particular, at $\text{IPC} = 50$, our approach achieves 84.2%, surpassing the strongest baseline by 0.5%.

ImageIDC. We further evaluate our method on the ImageIDC dataset, which contains classes with less similarity, using ResNet-18 as the backbone. As shown in Tab. 3, our method consistently achieves the best performance across all IPC settings. The improvement is most notable at $\text{IPC} = 1$, where our approach reaches 28.5%, outperforming the strongest baseline by 0.5%, demonstrating clear advantages in modeling the underlying distribution under extremely limited data budgets.

5.3 Analysis Experiments

We analyze three key hyperparameters and conduct ablation studies for our proposed method. Additional analysis results, including analysis of λ_{IM} and G , see Appendix.

Analysis on α and β . To further analyze the impact of the weighting coefficients in the subgroup selection objective, we conduct a sensitivity study on the parameters α and β in Eq. (10). Fig. 3 presents the accuracy heatmap obtained by varying α and β within the range $[0.1, 0.9]$. The results show that model performance remains stable across a wide range of parameter combinations, demonstrating the robustness of our method.

Ablation Studies. Tab. 4 presents the ablation results of IM and S^3 on ImageWoof and ImageNette under IPC settings of 10 and 50. Both components individually improve over the DiT baseline: IM expands distributional coverage, while S^3 strengthens inter-class separation during sampling. When combined as ImS^3 , the improvements are consistently larger across all settings.

Table 4. Ablation study of IM and S^3 under $\text{IPC} = 10$ and 50. Results on ImageWoof are obtained using ResNetAP-10, while results on ImageNette are obtained using ResNet-18. The best results are marked as bold.

Method	ImageWoof		ImageNette	
	IPC = 10	IPC = 50	IPC = 10	IPC = 50
DiT [23]	34.7±0.5	49.3±0.2	58.9±1.2	82.9±0.1
+ IM	37.3 ±0.1	53.5±0.5	60.0±0.9	81.5±0.5
+ S^3	40.9 ±0.2	54.9 ±0.5	62.2±1.9	81.3±1.2
+ ImS^3	41.8 ±0.3	61.0 ±0.7	62.9±1.2	84.2±1.0

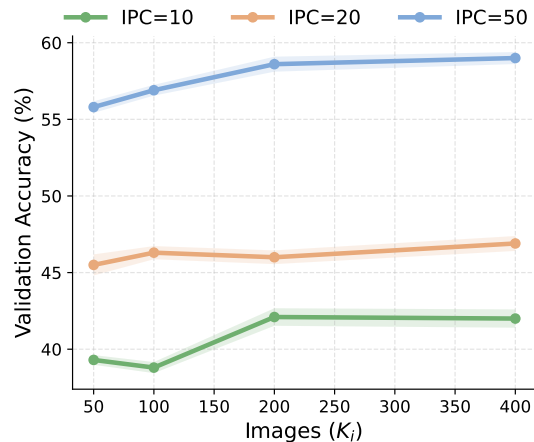


Figure 4. Analysis of real-images usage from original dataset used to compute reference centroids in Eq. (8). Moderate sample counts provide stable and reliable centroids for subgroup selection, while too few samples introduce noise and degrade selection quality.

Analysis on K_i . Fig. 4 examines the effect of the real-image budget K_i in Eq. (8) within our proposed S^3 . We conduct experiments on ResNetAP-10 under $\text{IPC} = 10, 20$, and 50. The result demonstrates that use more images to compute centroids stabilizes the reference distribution and consistently improves the quality of the selected subgroups, especially under high IPC setting.

6 Conclusion

We propose ImS^3 , a simple yet effective two-stage framework for large-scale dataset distillation, addressing two critical issues in diffusion-based approaches: insufficient distribution coverage and weak discriminative diversity. Our method achieves state-of-the-art performance across multiple benchmarks, including ImageWoof, ImageNette, ImageIDC, and ImageNet, under various evaluation settings. By combining inversion-guided fine-tuning with centroid-based sampling, ImS^3 provides a new perspective and a practical solution for improving diffusion-based dataset distillation.

Acknowledgement

This work was supported by the National Natural Science Foundation of China (No. 6250070674) and the Zhejiang Leading Innovative and Entrepreneur Team Introduction Program (2024R01007). This work was also supported by the National Research Foundation, Singapore and Infocomm Media Development Authority under its Trust Tech Funding Initiative. Any opinions, findings and conclusions or recommendations expressed in this material are those of the author(s) and do not reflect the views of the National Research Foundation, Singapore and Infocomm Media Development Authority.

References

- [1] Giulio Biroli, Tony Bonnaire, Valentin De Bortoli, and Marc Mézard. Dynamical regimes of diffusion models. *Nature Communications*, 15(1):9957, 2024. 2
- [2] George Cazenavette, Tongzhou Wang, Antonio Torralba, Alexei A Efros, and Jun-Yan Zhu. Dataset distillation by matching training trajectories. In *Proceedings of the IEEE/CVF Conference on Computer Vision and Pattern Recognition*, pages 4750–4759, 2022. 1, 3
- [3] Jeffrey A. Chan-Santiago, Praveen Tirupattur, Gaurav Kumar Nayak, Gaowen Liu, and Mubarak Shah. Mgd³: Mode-guided dataset distillation using diffusion models, 2025. 2, 1
- [4] Mingyang Chen, Jiawei Du, Bo Huang, Yi Wang, Xiaobo Zhang, and Wei Wang. Influence-guided diffusion for dataset distillation. In *The Thirteenth International Conference on Learning Representations*, 2025. 2
- [5] Yingying Deng, Xiangyu He, Changwang Mei, Peisong Wang, and Fan Tang. Fireflow: Fast inversion of rectified flow for image semantic editing, 2024. 3
- [6] Zhiwei Deng and Olga Russakovsky. Remember the past: distilling datasets into addressable memories for neural networks. In *Proceedings of the 36th International Conference on Neural Information Processing Systems*, Red Hook, NY, USA, 2022. Curran Associates Inc. 1
- [7] Jiahui Geng, Zongxiong Chen, Yuandou Wang, Herbert Woitschläger, Sonja Schimmler, Ruben Mayer, Zhiming Zhao, and Chunming Rong. A survey on dataset distillation: approaches, applications and future directions. In *Proceedings of the Thirty-Second International Joint Conference on Artificial Intelligence*, 2023. 1
- [8] Jianyang Gu, Saeed Vahidian, Vyacheslav Kungurtsev, Haonan Wang, Wei Jiang, Yang You, and Yiran Chen. Efficient dataset distillation via minimax diffusion. In *Proceedings of the IEEE/CVF Conference on Computer Vision and Pattern Recognition*, pages 15793–15803, 2024. 1, 2, 3, 5, 7, 4, 6, 8, 9, 10, 11, 12, 13, 14, 15, 16, 17
- [9] Jonathan Ho, Ajay Jain, and Pieter Abbeel. Denoising diffusion probabilistic models, 2020. 2
- [10] Jeremy Howard. Imagenette: A smaller subset of 10 easily classified classes from imagenet, 2019. 6
- [11] Jeremy Howard. Imagewoof: a subset of 10 classes from imagenet that aren’t so easy to classify, 2019. 6
- [12] Xuan Ju, Ailing Zeng, Yuxuan Bian, Shaoteng Liu, and Qiang Xu. Pnp inversion: Boosting diffusion-based editing with 3 lines of code. *International Conference on Learning Representations (ICLR)*, 2024. 3
- [13] Rafał Karczewski, Markus Heinonen, and Vikas Garg. Diffusion models as cartoonists: The curious case of high density regions, 2025. 2
- [14] Jang-Hyun Kim, Jinuk Kim, Seong Joon Oh, Sangdoon Yun, Hwanjun Song, Joonhyun Jeong, Jung-Woo Ha, and Hyun Oh Song. Dataset condensation via efficient synthetic-data parameterization, 2022. 1, 6, 7, 2
- [15] Diederik P. Kingma and Ruiqi Gao. Understanding diffusion objectives as the elbo with simple data augmentation, 2023. 2
- [16] Yann LeCun, Yoshua Bengio, and Geoffrey Hinton. Deep learning. *nature*, 521(7553):436–444, 2015. 1
- [17] Noel Loo, Ramin Hasani, Alexander Amini, and Daniela Rus. Efficient dataset distillation using random feature approximation. *Advances in Neural Information Processing Systems*, 35:13877–13891, 2022. 1
- [18] Cheng Lu, Yuhao Zhou, Fan Bao, Jianfei Chen, Chongxuan Li, and Jun Zhu. Dpm-solver: A fast ode solver for diffusion probabilistic model sampling in around 10 steps, 2022. 2
- [19] Cheng Lu, Yuhao Zhou, Fan Bao, Jianfei Chen, Chongxuan Li, and Jun Zhu. Dpm-solver++: Fast solver for guided sampling of diffusion probabilistic models. *Machine Intelligence Research*, 22(4):730–751, 2025. 2
- [20] Ron Mokady, Amir Hertz, Kfir Aberman, Yael Pritch, and Daniel Cohen-Or. Null-text inversion for editing real images using guided diffusion models. In *Proceedings of the IEEE/CVF Conference on Computer Vision and Pattern Recognition (CVPR)*, pages 6038–6047, 2023. 2, 3
- [21] Brian B. Moser, Federico Raue, Sebastian Palacio, Stanislav Frolov, and Andreas Dengel. Unlocking dataset distillation with diffusion models, 2025. 2
- [22] Timothy Nguyen, Zhoung Chen, and Jaehoon Lee. Dataset meta-learning from kernel ridge-regression. *arXiv preprint arXiv:2011.00050*, 2020. 2
- [23] William Peebles and Saining Xie. Scalable diffusion models with transformers. *arXiv preprint arXiv:2212.09748*, 2022. 1, 4, 5, 6, 7, 8
- [24] L Rout, Y Chen, N Ruiz, C Caramanis, S Shakkottai, and W Chu. Semantic image inversion and editing using rectified stochastic differential equations. In *The Thirteenth International Conference on Learning Representations*, 2025. 3
- [25] Olga Russakovsky, Jia Deng, Hao Su, Jonathan Krause, Sanjeev Satheesh, Sean Ma, Zhiheng Huang, Andrej Karpathy, Aditya Khosla, Michael Bernstein, Alexander C. Berg, and Li Fei-Fei. ImageNet Large Scale Visual Recognition Challenge. *International Journal of Computer Vision (IJCV)*, 115(3):211–252, 2015. 1, 6
- [26] Naveen Sachdeva and Julian McAuley. Data distillation: A survey, 2023. 1
- [27] Ahmad Sajedi, Samir Khaki, Ehsan Amjadian, Lucy Z. Liu, Yuri A. Lawryshyn, and Konstantinos N. Plataniotis. Datadam: Efficient dataset distillation with attention matching, 2025. 1

- [28] Ozan Sener and Silvio Savarese. Active learning for convolutional neural networks: A core-set approach, 2018. 7
- [29] Shitong Shao, Zeyuan Yin, Muxin Zhou, Xindong Zhang, and Zhiqiang Shen. Generalized large-scale data condensation via various backbone and statistical matching. In *Proceedings of the IEEE/CVF Conference on Computer Vision and Pattern Recognition*, pages 16709–16718, 2024. 3
- [30] Jiaming Song, Chenlin Meng, and Stefano Ermon. Denoising diffusion implicit models. *arXiv:2010.02502*, 2020. 2, 3
- [31] Yang Song, Jascha Sohl-Dickstein, Diederik P. Kingma, Abhishek Kumar, Stefano Ermon, and Ben Poole. Score-based generative modeling through stochastic differential equations, 2021. 2
- [32] Duo Su, Junjie Hou, Weizhi Gao, Yingjie Tian, and Bowen Tang. D^4 : Dataset distillation via disentangled diffusion model. In *Proceedings of the IEEE/CVF Conference on Computer Vision and Pattern Recognition*, pages 5809–5818, 2024. 2, 3, 7
- [33] Peng Sun, Bei Shi, Daiwei Yu, and Tao Lin. On the diversity and realism of distilled dataset: An efficient dataset distillation paradigm. In *Proceedings of the IEEE/CVF Conference on Computer Vision and Pattern Recognition (CVPR)*, 2024. 7, 2, 3
- [34] Peng Sun, Bei Shi, Daiwei Yu, and Tao Lin. On the diversity and realism of distilled dataset: An efficient dataset distillation paradigm. In *2024 IEEE/CVF Conference on Computer Vision and Pattern Recognition (CVPR)*, pages 9390–9399, 2024. 7
- [35] Yonglong Tian, Dilip Krishnan, and Phillip Isola. Contrastive multiview coding. In *Computer Vision—ECCV 2020: 16th European Conference, Glasgow, UK, August 23–28, 2020, Proceedings, Part XI 16*, pages 776–794. Springer, 2020. 6
- [36] Chenru Wang, Beier Zhu, and Chi Zhang. Free lunch for stabilizing rectified flow inversion, 2026. 2
- [37] Haoxuan Wang, Zhenghao Zhao, Junyi Wu, Yuzhang Shang, Gaowen Liu, and Yan Yan. Cao2: Rectifying inconsistencies in diffusion-based dataset distillation. In *Proceedings of the IEEE/CVF International Conference on Computer Vision (ICCV)*, pages 4722–4731, 2025. 2, 7, 3
- [38] Jiangshan Wang, Junfu Pu, Zhongang Qi, Jiayi Guo, Yue Ma, Nisha Huang, Yuxin Chen, Xiu Li, and Ying Shan. Taming rectified flow for inversion and editing. *arXiv preprint arXiv:2411.04746*, 2024. 3
- [39] Kai Wang, Zekai Li, Zhi-Qi Cheng, Samir Khaki, Ahmad Sajedi, Ramakrishna Vedantam, Konstantinos N Plataniotis, Alexander Hauptmann, and Yang You. Emphasizing discriminative features for dataset distillation in complex scenarios, 2025. 1
- [40] Tongzhou Wang, Jun-Yan Zhu, Antonio Torralba, and Alexei A Efros. Dataset distillation. *arXiv preprint arXiv:1811.10959*, 2018. 1, 3
- [41] Max Welling. Herding dynamical weights to learn. In *Proceedings of the 26th annual international conference on machine learning*, pages 1121–1128, 2009. 7, 1, 2
- [42] Huyu Wu, Duo Su, Junjie Hou, and Guang Li. Dataset condensation with color compensation, 2025. 2
- [43] Enze Xie, Lewei Yao, Han Shi, Zhili Liu, Daquan Zhou, Zhaoqiang Liu, Jiawei Li, and Zhenguo Li. Diffit: Unlocking transferability of large diffusion models via simple parameter-efficient fine-tuning, 2023. 5, 6
- [44] Zeyuan Yin and Zhiqiang Shen. Dataset distillation in large data era. *arXiv preprint arXiv:2311.18838*, 2023. 3
- [45] Zeyuan Yin, Eric Xing, and Zhiqiang Shen. Squeeze, recover and relabel: Dataset condensation at imagenet scale from a new perspective. *Advances in Neural Information Processing Systems*, 36:73582–73603, 2023. 3, 7
- [46] Han Zhang, Jinghong Mao, Shangwen Zhu, Zhantao Yang, Lianghua Huang, Yu Liu, Deli Zhao, Ruili Feng, and Fan Cheng. Instability in diffusion odes: An explanation for inaccurate image reconstruction, 2025. 2, 3, 4, 1
- [47] Bo Zhao and Hakan Bilen. Dataset condensation with distribution matching. In *Proceedings of the IEEE/CVF Winter Conference on Applications of Computer Vision*, pages 6514–6523, 2023. 7
- [48] Bo Zhao and Hakan Bilen. Dataset condensation with distribution matching. In *Proceedings of the IEEE/CVF Winter Conference on Applications of Computer Vision*, pages 6514–6523, 2023. 1
- [49] Bo Zhao, Konda Reddy Mopuri, and Hakan Bilen. Dataset condensation with gradient matching. *arXiv preprint arXiv:2006.05929*, 2020. 1, 2, 3
- [50] Lin Zhao, Yushu Wu, Xinru Jiang, Jianyang Gu, Yanzhi Wang, Xiaolin Xu, Pu Zhao, and Xue Lin. Taming diffusion for dataset distillation with high representativeness. *arXiv preprint arXiv:2505.18399*, 2025. 2, 3, 7
- [51] Muxin Zhou, Zeyuan Yin, Shitong Shao, and Zhiqiang Shen. Self-supervised dataset distillation: A good compression is all you need. *arXiv preprint arXiv:2404.07976*, 2024. 3
- [52] Yongchao Zhou, Ehsan Nezhadarya, and Jimmy Ba. Dataset distillation using neural feature regression. *Advances in Neural Information Processing Systems*, 35:9813–9827, 2022. 1
- [53] Yawen Zou, Guang Li, Duo Su, Zi Wang, Jun Yu, and Chao Zhang. Dataset distillation via vision-language category prototype. *arXiv preprint arXiv:2506.23580*, 2025. 2, 3, 7

IMS3: Breaking Distributional Aggregation in Diffusion-Based Dataset Distillation

Supplementary Material

Contents

7. Instability in Inversion	1
8. More Experiments	1
8.1. Comparison on ImageNet-100	1
8.2. Experiment Results on Different Student Model	2
8.3. Analysis on Loss Functions	2
8.4. Analysis on λ_{IM}	2
8.5. Analysis on G	2
8.6. Analysis on Feature Extractors for Centroid Selection	3
8.7. t-SNE Visualization on ImageNet-100	3
8.8. Runtime Analysis	4
8.9. Higher Resolution (512×512).	4
8.10 ViT Architecture Evaluation.	4
8.11 ImageNet-1K Experiments.	4
8.12 Decision Boundary Visualization.	4
8.13 Real Data Accessibility	4
9. Visualization	4

7. Instability in Inversion

Diffusion inversion theoretically provides a deterministic mapping between real data and their latent noises by integrating the probability flow ODE (PF-ODE) backward in time. However, recent work reveals that this inversion process is inherently unstable in high-dimensional spaces [46]. Specifically, even infinitesimal perturbations in the latent space can be amplified through the ODE dynamics, leading to substantial reconstruction errors during the forward regeneration process.

Formally, let $F : \mathbb{R}^n \rightarrow \mathbb{R}^n$ denote the PF-ODE mapping from noise to data. The instability of F can be characterized by the geometric mean of its singular values, known as the *geometric mean instability coefficient*:

$$\bar{\mathcal{E}}_F(\mathbf{z}) = \left(\prod_{i=1}^n \frac{\|J_F(\mathbf{z}) \mathbf{u}_i\|_2}{\|\mathbf{u}_i\|_2} \right)^{1/n}, \quad (12)$$

where $J_F(\mathbf{z})$ denotes the Jacobian matrix of F at \mathbf{z} and $\{\mathbf{u}_i\}$ are orthonormal basis vectors. When $\bar{\mathcal{E}}_F(\mathbf{z}) > 1$, the mapping locally expands the volume element around \mathbf{z} , implying that infinitesimal perturbations will be amplified after propagation through F .

To quantify the probability that such instability occurs, they establish the following lower bound for any threshold

$M > 1$:

$$\mathcal{P}_M := \pi_{\text{real}}(\{\mathbf{z} : \bar{\mathcal{E}}_F(F^{-1}(\mathbf{z})) > M\}) \geq 1 - \epsilon - \delta, \quad (13)$$

where

$$\begin{aligned} \epsilon &:= \pi_{\text{real}}\left(\left\{\mathbf{z} : p_{\text{gen}}(\mathbf{z}) \geq \frac{1}{(2\pi M^2)^{n/2}} e^{-\frac{2n+3\sqrt{2n}}{2}}\right\}\right), \\ \delta &:= \pi_{\text{real}}\left(\left\{\mathbf{z} : \|F^{-1}(\mathbf{z})\|^2 > 2n + 3\sqrt{2n}\right\}\right). \end{aligned} \quad (14)$$

Here, π_{real} denotes the real data distribution, and p_{gen} represents the generation distribution of the diffusion model. As dimensionality n increases, both ϵ and δ vanish, implying that the instability probability \mathcal{P}_M approaches one—thus instability becomes almost inevitable in high-dimensional diffusion mappings.

Intuitively, this phenomenon arises from the sparsity of the generation distribution. Since the generative probability mass is concentrated in a few narrow regions while most of the space exhibits near-zero density, the PF-ODE must stretch the mapping to preserve probability. Consequently, regions of low density in the generative space correspond to large local Jacobian norms, leading to the amplification of any perturbation during inversion or regeneration. This explains why inversion trajectories often drift toward low-density, high-sensitivity regions of the data manifold, as also observed in Sec. 4.1. A more detailed mathematical derivation and discussion of the instability mechanism can be found in [46].

This inherent instability directly motivates the design of our Inversion-Matching fine-tuning (IM) in ImS³. Rather than viewing instability as an obstacle, we exploit it as a guiding property to drive the diffusion model toward low-density regions.

By aligning the denoising trajectory with the inversion trajectory, our method explicitly leverages the instability-induced drift to expand the distributional coverage and enhance representation diversity in the distilled dataset.

8. More Experiments

8.1. Comparison on ImageNet-100

Tab. 5 reports the comparison across different IPC and backbone on ImageNet-100. Across all settings, our method consistently delivers the highest accuracy, outperforming existing approaches such as Herding [41], IDC-1 [14], Minimax [8], and MGD³ [3].

Table 5. Performance comparison on ImageNet-100 under different IPC and backbone settings. Results are Top-1 accuracy.

IPC	Model	Random	Herding [41]	IDC-1 [14]	Minimax [14]	MGD ³ [3]	ImS ³ (Ours)
10	ConvNet-6	17.0 \pm 0.3	17.2 \pm 0.3	24.3 \pm 0.5	22.3 \pm 0.5	23.4 \pm 0.9	24.3\pm1.1
	ResNetAP-10	19.1 \pm 0.4	19.8 \pm 0.3	25.7 \pm 0.1	24.8 \pm 0.2	25.8 \pm 0.5	28.4\pm0.2
	ResNet-18	17.5 \pm 0.5	16.1 \pm 0.2	25.1 \pm 0.2	22.5 \pm 0.3	23.6 \pm 0.4	28.3\pm0.3
20	ConvNet-6	24.8 \pm 0.2	24.3 \pm 0.4	28.8 \pm 0.3	29.3 \pm 0.4	30.6 \pm 0.4	30.7\pm0.4
	ResNetAP-10	26.7 \pm 0.5	27.6 \pm 0.1	29.9 \pm 0.2	32.3 \pm 0.1	33.9 \pm 1.1	34.8\pm0.2
	ResNet-18	25.5 \pm 0.3	24.7 \pm 0.1	30.2 \pm 0.2	31.2 \pm 0.1	32.6 \pm 0.4	36.3\pm0.2

8.2. Experiment Results on Different Student Model

Tab. 6 reports the performance of different dataset distillation methods on ImageWoof across multiple backbone architectures, including ResNet-18, ResNet-50, ResNet-101, and multiple IPC settings. Across all configurations, our method achieves the highest accuracy, demonstrating clear and consistent advantages in both low- and high-budget regimes. The improvements are particularly notable under low IPC (e.g., IPC = 10), where the limited data makes representation learning more challenging: ImS³ boosts ResNet-18 performance from 45.6% (CaO²) to 45.9%, and ResNet-50 accuracy from 40.1% to 42.7%. Under higher IPC (IPC = 50), ImS³ continues to outperform strong baselines such as Minimax [8], RDED [33], and CaO² [37], confirming that our approach generalizes well across model capacities and data regimes. These results highlight the robustness and scalability of ImS³ for improving distilled dataset quality on large-scale visual recognition tasks.

8.3. Analysis on Loss Functions

Table 7 presents an ablation study on different similarity losses used in IM. We evaluate three widely used losses L_1 , L_2 , and $1 - \sigma$ in Sec. 4.1 on ImageWoof and ImageNette under IPC = 10 and 50. Both L_1 and L_2 exhibit comparable performance, providing moderate improvements across IPC settings. In contrast, the proposed $1 - \sigma$ formulation consistently achieves the highest accuracy, surpassing the other two losses by a clear margin at both data budgets. These results highlight the importance of treating feature deviations in a distribution-aware manner, suggesting that the $1 - \sigma$ -based loss stabilizes inversion alignment and leads to more reliable distilled samples.

8.4. Analysis on λ_{IM}

To examine the sensitivity of our method to the matching strength, we perform a sweep over λ_{IM} and report the validation accuracy for IPC = 10, 20, and 50 in Fig. 5). Across all settings, the performance remains stable within a broad interval of λ_{IM} , indicating that the method is not overly sensitive to this hyperparameter. For smaller coefficients (e.g.,

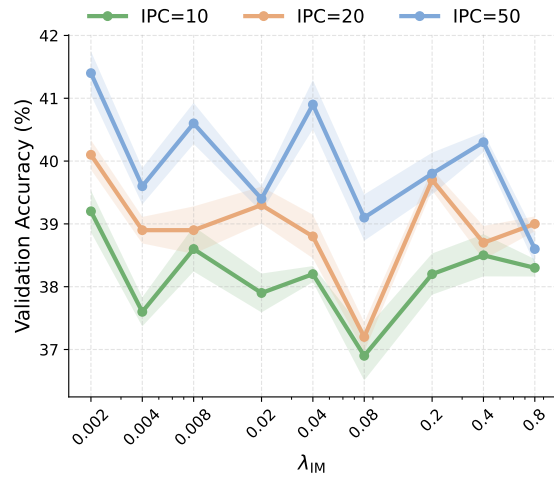


Figure 5. Validation accuracy under different matching strengths. Performance of our method across a range of matching coefficients λ_{IM} for IPC = 10, 20, and 50. Each curve corresponds to a fixed IPC, and shaded regions denote performance variability across runs.

2×10^{-3} to 8×10^{-3}), the accuracy stays consistently high, especially at IPC = 50. When λ_{IM} becomes excessively large (e.g., 0.4–0.8), the accuracy gradually drops, likely because overly strong alignment introduces optimization bias and reduces the diversity of the distilled samples.

8.5. Analysis on G

We analyze the effect of the subgroup pool size G , which determines how many candidate subgroups are generated for each class before selection. As shown in Fig. 6, increasing G helps expose more inter-class variability and improves distilled accuracy when the IPC is small, since low-data regimes benefit from a richer candidate pool. However, the trend does not extend indefinitely: overly large pools introduce redundant or low-quality samples, weakening the discriminative structure and causing performance to decline. This highlights the need to choose G according to the IPC setting, where lower IPC typically requires a larger

Table 6. Performance comparison under different IPC and backbone settings on ImageWoof. Best results in each setting are marked as bold.

Backbone	IPC	SRe ² L [45]	Minimax [8]	RDED [33]	CaO ² [37]	ImS ³ (Ours)
ResNet-18	10	20.2 \pm 0.2	40.1 \pm 1.0	38.5 \pm 2.1	45.6 \pm 1.4	45.9\pm1.3
	50	23.3 \pm 0.3	67.0 \pm 1.8	68.5 \pm 0.7	68.9 \pm 1.1	71.2\pm1.3
ResNet-50	10	17.3 \pm 1.7	37.3 \pm 1.1	29.9 \pm 2.2	40.1 \pm 0.1	42.7\pm1.8
	50	24.8 \pm 0.7	64.3 \pm 0.9	67.8 \pm 0.3	68.2 \pm 1.1	68.3\pm0.2
ResNet-101	10	17.7 \pm 0.9	34.2 \pm 1.7	31.3 \pm 1.3	36.5 \pm 1.4	38.2\pm1.6
	50	21.2 \pm 0.2	62.7 \pm 1.6	59.1 \pm 0.7	63.1 \pm 1.3	66.1\pm1.8

Table 7. Ablation study of different similarity losses used in the IM on ImageWoof and ImageNette under IPC = 10 and 50. Results are reported as top-1 accuracy.

Loss Type	ImageWoof		ImageNette	
	IPC = 10	IPC = 50	IPC = 10	IPC = 50
L_1	38.7 \pm 0.2	58.1 \pm 0.2	62.6 \pm 0.9	81.7 \pm 0.7
L_2	39.0 \pm 0.2	58.1 \pm 0.1	62.7 \pm 1.0	82.8 \pm 0.7
$1 - \sigma$	41.8\pm0.3	60.1\pm0.7	62.9\pm1.2	84.2\pm1.0

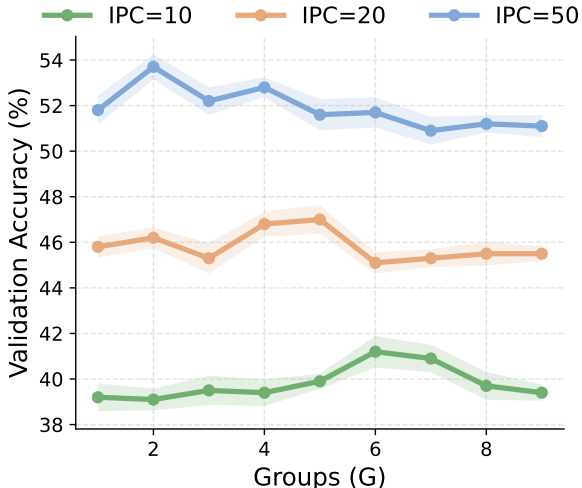


Figure 6. Effect of subgroup pool size G under different IPC settings on ImageWoof. A moderate increase in G provides richer intra-class variation and improves selection quality, especially in low-IPC regimes. However, excessively large pools introduce redundant or noisy candidates, which destabilizes selection and leads to degraded performance.

pool while higher IPC benefits less from further expansion.

8.6. Analysis on Feature Extractors for Centroid Selection

To further investigate the robustness of our centroid-based subgroup selection, we replace the default ResNet-18 feature extractor with different backbones, including ResNet-50, ResNet-101, EfficientNet, and CLIP. We report the distilled top-1 accuracy on ImageWoof under IPC = 10 and 20.

Table 8. Ablation study on feature extractors for centroid selection on ImageWoof. Top-1 accuracy (%).

IPC	Res18	Res50	Res101	Efficient	CLIP
10	41.8\pm0.3	39.6 \pm 0.3	38.8 \pm 0.2	39.5 \pm 0.2	38.1 \pm 0.5
20	45.8\pm1.2	45.7 \pm 0.3	45.0 \pm 0.2	45.8 \pm 0.3	44.3 \pm 0.2

Across both settings, we observe that the choice of feature extractor has noticeable impact on the quality of sampling process. The results do not follow the conventional expectation that deeper backbones always yield better distilled results. Instead, the lightweight ResNet-18 achieves the highest top-1 accuracy among both IPC budgets. It implies that moderate capacity features provide a more stable and suitable embedding space for centroid sampling procedure.

8.7. t-SNE Visualization on ImageNet-100

To further examine how our method shapes the feature distribution of the distilled dataset, we visualize the embeddings of synthesized samples using t-SNE on ImageNet-100. We compare our approach (ImS³) with MinimaxD-diffusion, and the results are shown in Fig. 8. Each color corresponds to a different class.

As illustrated by the comparison, ImS³ produces significantly more compact and well-structured intra-class clusters. Points belonging to the same class exhibit tighter grouping, indicating that our inversion-matching mechanism encourages stronger within-class consistency. More-

over, ImS^3 demonstrates clearer separation between different classes, suggesting that the synthesized samples form a more discriminative embedding structure. This indicates that our distribution-aware feature alignment promotes both intra-class cohesion and inter-class separability, which are crucial properties for effective dataset distillation.

In contrast, MinimaxDiffusion yields more fragmented and overlapping clusters. Classes become less compact and boundaries are looser, implying weaker semantic organization in the distilled data. The tighter clustering and improved class separation produced by ImS^3 provide intuitive evidence that our method captures the intrinsic class geometry more faithfully, leading to improved downstream recognition performance.

8.8. Runtime Analysis

We report runtime on a single RTX 4090 GPU using ImageWoof. As shown in Table 9, IM requires only 8 epochs of fine-tuning, while S^3 sampling is training-free, resulting in competitive total runtime.

Table 9. Runtime comparison on ImageWoof (IPC=10).

	DiT	Minimax	MGD3	IMS^3
Fine-tuning	-	32min	-	19.5min
Sampling	1.5min	1.5min	21min	7min
Total	1.5min	33.5min	21min	26.5min

8.9. Higher Resolution (512×512).

We evaluate IMS^3 at 512×512 using DiT-XL/2-512. Table 10 reports consistent advantages at IPC=10 and IPC=50.

Table 10. 512×512 results on ImageWoof.

	DiT	Minimax	CaO ²	IMS^3
IPC=10	36.6±0.2	33.3±0.2	37.5±0.3	37.9±0.2
IPC=50	52.5±0.2	51.4±0.5	53.8±0.6	59.6±0.3

8.10. ViT Architecture Evaluation.

We evaluate distilled datasets on ViT and EfficientNet. As shown in Table 11, IMS^3 improves results under both architectures, indicating good transfer across classifier families.

8.11. ImageNet-1K Experiments.

We evaluate IMS^3 on full ImageNet-1K. Table 12 reports results.

8.12. Decision Boundary Visualization.

We visualize classifier features using t-SNE in Figure 7. Samples selected by IMS^3 are closer to the decision boundaries.

Table 11. Cross-architecture evaluation on ImageWoof.

	Model	Minimax	MGD3	IMS^3
IPC=10	EfficientNet	31.3±0.7	32.3±0.3	34.2±0.2
	ViT	18.9±0.0	17.7±0.2	20.0±0.0
IPC=50	EfficientNet	46.3±1.0	49.3±0.5	51.7±0.4
	ViT	18.8±0.3	17.6±0.1	19.9±0.5

Table 12. ImageNet-1K results (IPC=10).

	SRe ² L	RDED	Minimax	MGD3	IMS^3
Top-1 Acc.	21.3±0.6	42.0±0.1	44.3±0.5	45.5±0.1	45.6±0.3

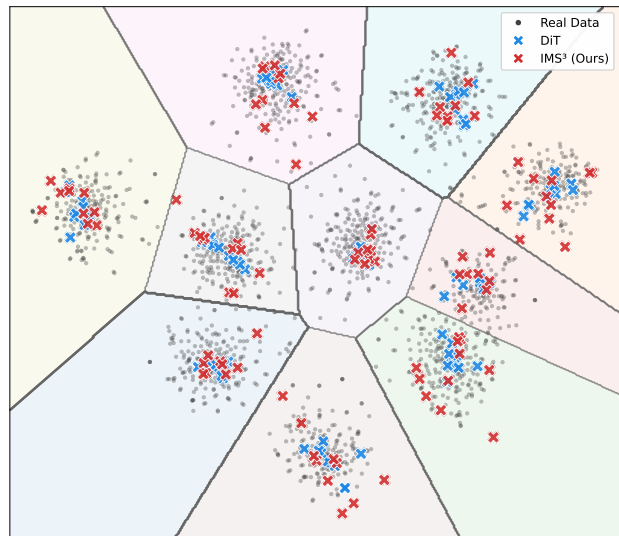


Figure 7. Feature-space visualization of distilled samples.

8.13. Real Data Accessibility

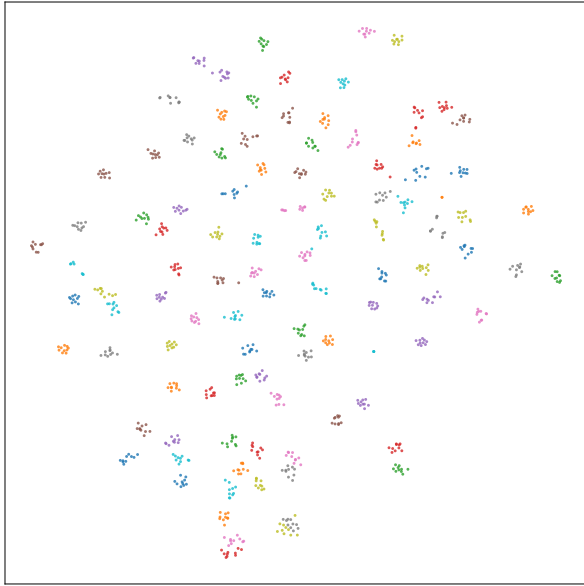
S^3 can approximate class centroids using samples generated by the diffusion model itself. As shown in Table 13, using generated samples to estimate centroids still effective compared to the baselines.

Table 13. Gen-data centroid results on ImageWoof

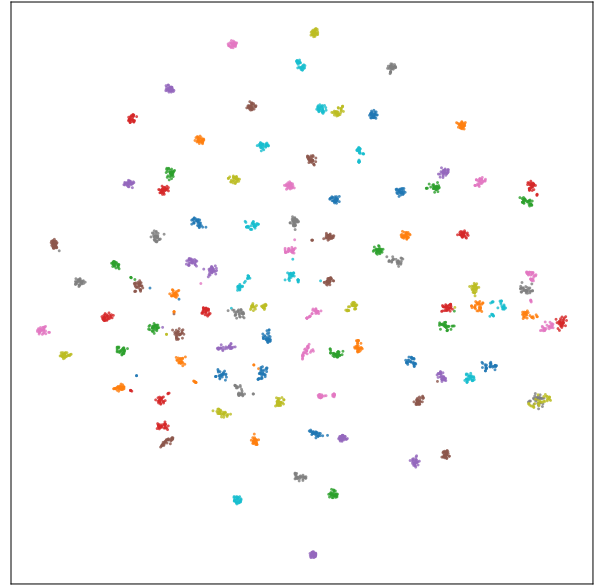
	DiT	Minimax	$\text{IMS}^3_{\text{Gen}}$	$\text{IMS}^3_{\text{Real}}$
IPC=10	34.7±0.5	35.7±0.3	<u>39.6±0.4</u>	41.8±0.3
IPC=50	49.3±0.2	54.4±0.6	<u>55.5±0.3</u>	57.3±0.5

9. Visualization

We demonstrate the samples selected by Minimax [8] and ImS^3 , Fig. 9 is the distilled samples from ImageWoof, Fig. 10 is the distilled samples from ImageNette, and



(a) ImageNet-100: ImS^3 (ours)



(b) ImageNet-100: MinimaxDiffusion

Figure 8. t-SNE visualization of distilled samples on ImageNet-100 and ImageWoof. ImS^3 produces tighter intra-class clusters and clearer inter-class separation, whereas MinimaxDiffusion exhibits more dispersed and overlapping structures.

Figs. 11 to 20 are the distilled samples from ImageNet-100.

MinimaxDiffusion

IMS³

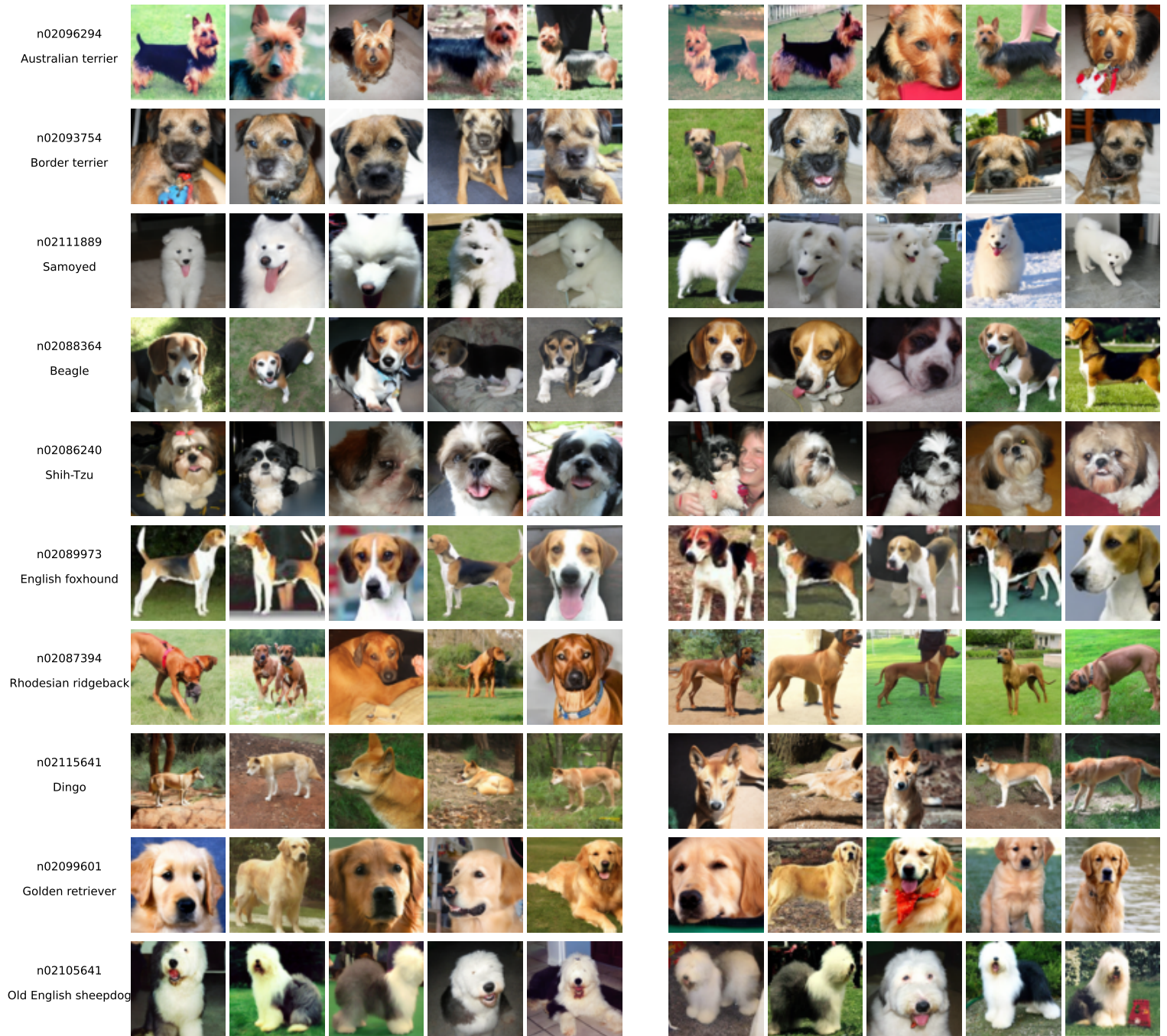


Figure 9. Comparison between samples selected by Minimax [8] (left) and generated by the proposed ImS^3 (right) for ImageWoof. The class names are marked at the left of each row.

MinimaxDiffusion

IMS³

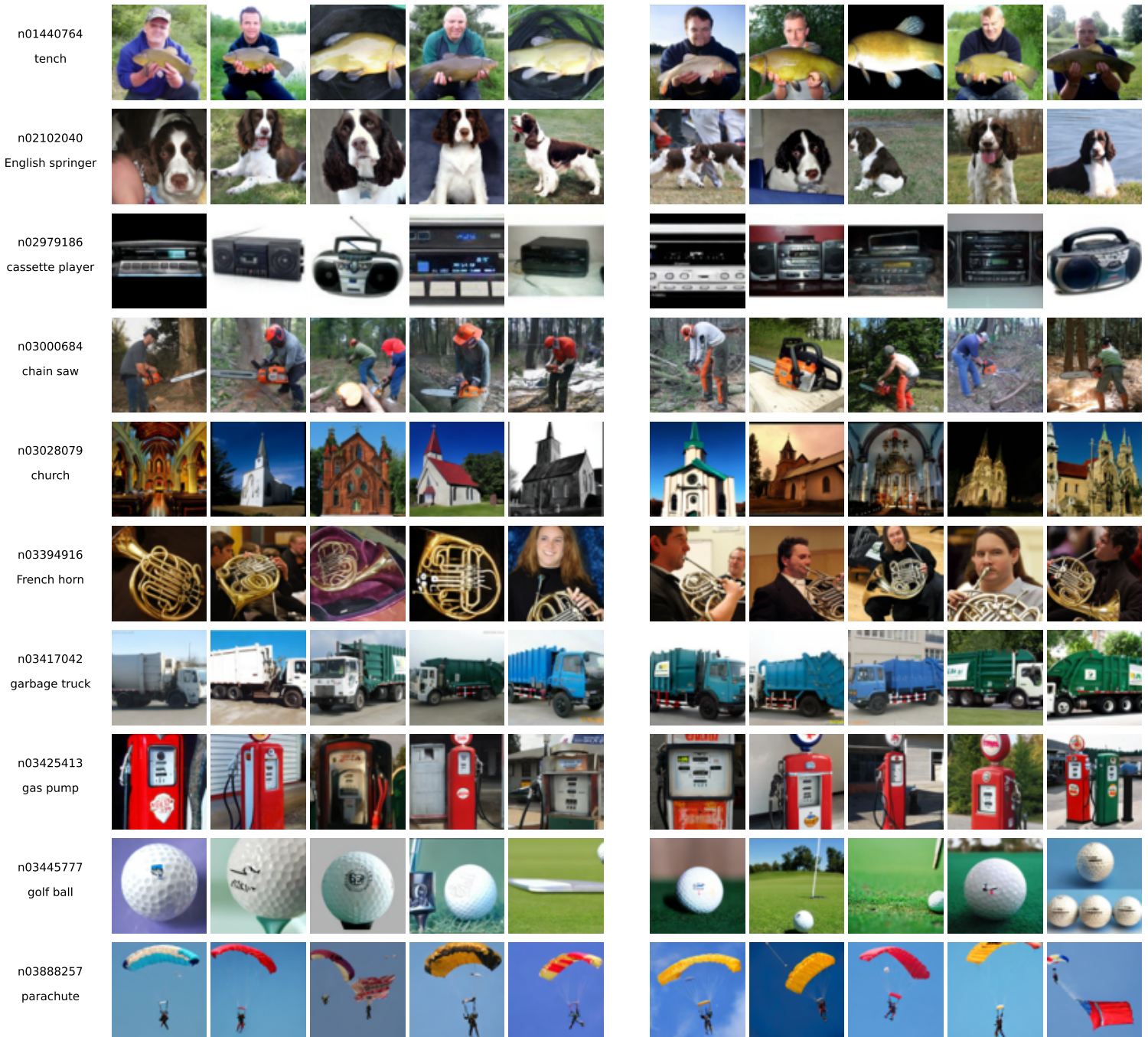


Figure 10. Comparison between samples selected by Minimax [8] (left) and generated by the proposed ImS^3 (right) for ImageNette. The class names are marked at the left of each row.

MinimaxDiffusion

IMS³

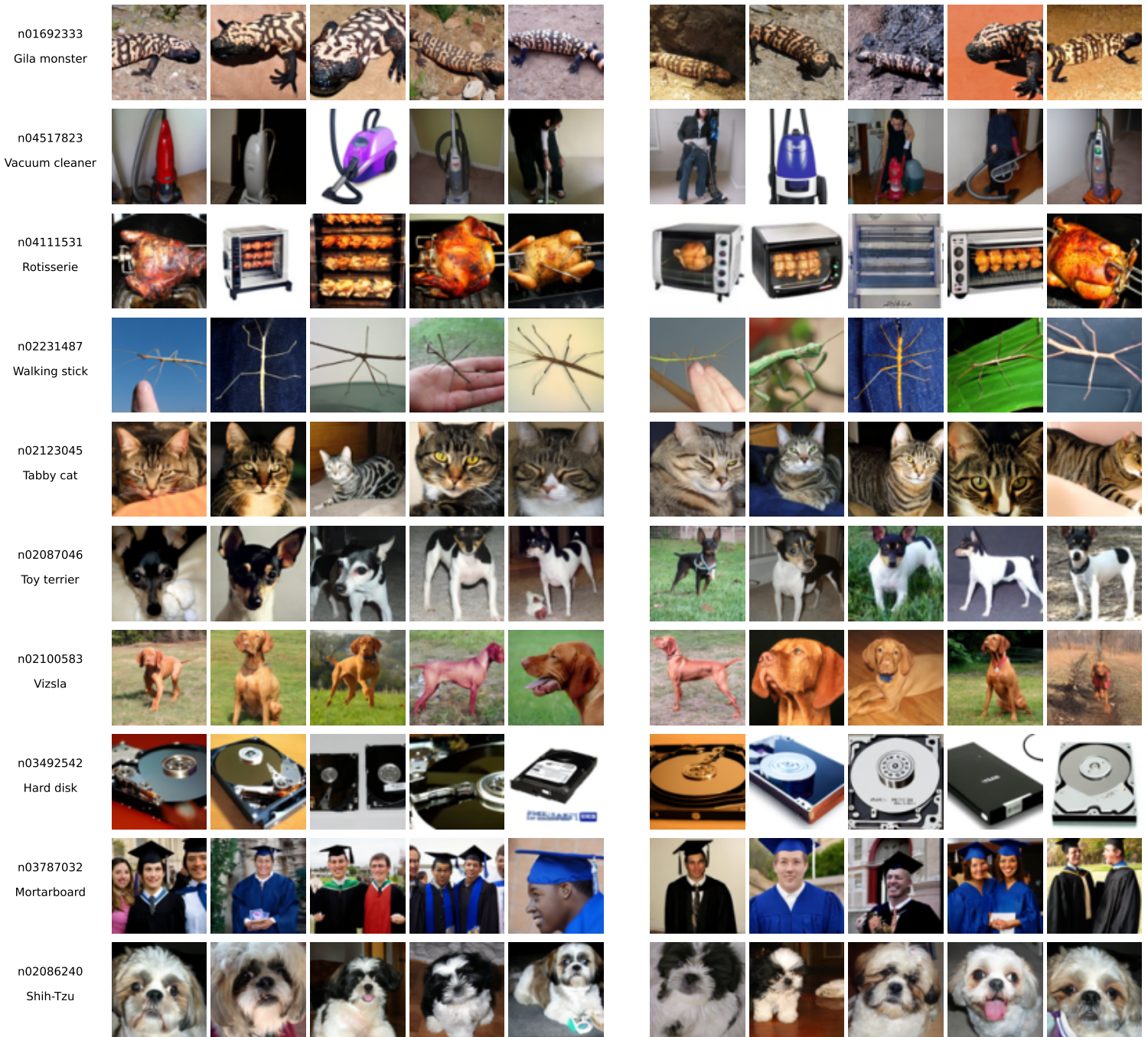


Figure 11. Comparison between samples selected by Minimax [8] (left) and generated by the proposed ImS³ (right) for ImageNet-100 classes 0-9. The class names are marked at the left of each row.

MinimaxDiffusion

IMS³

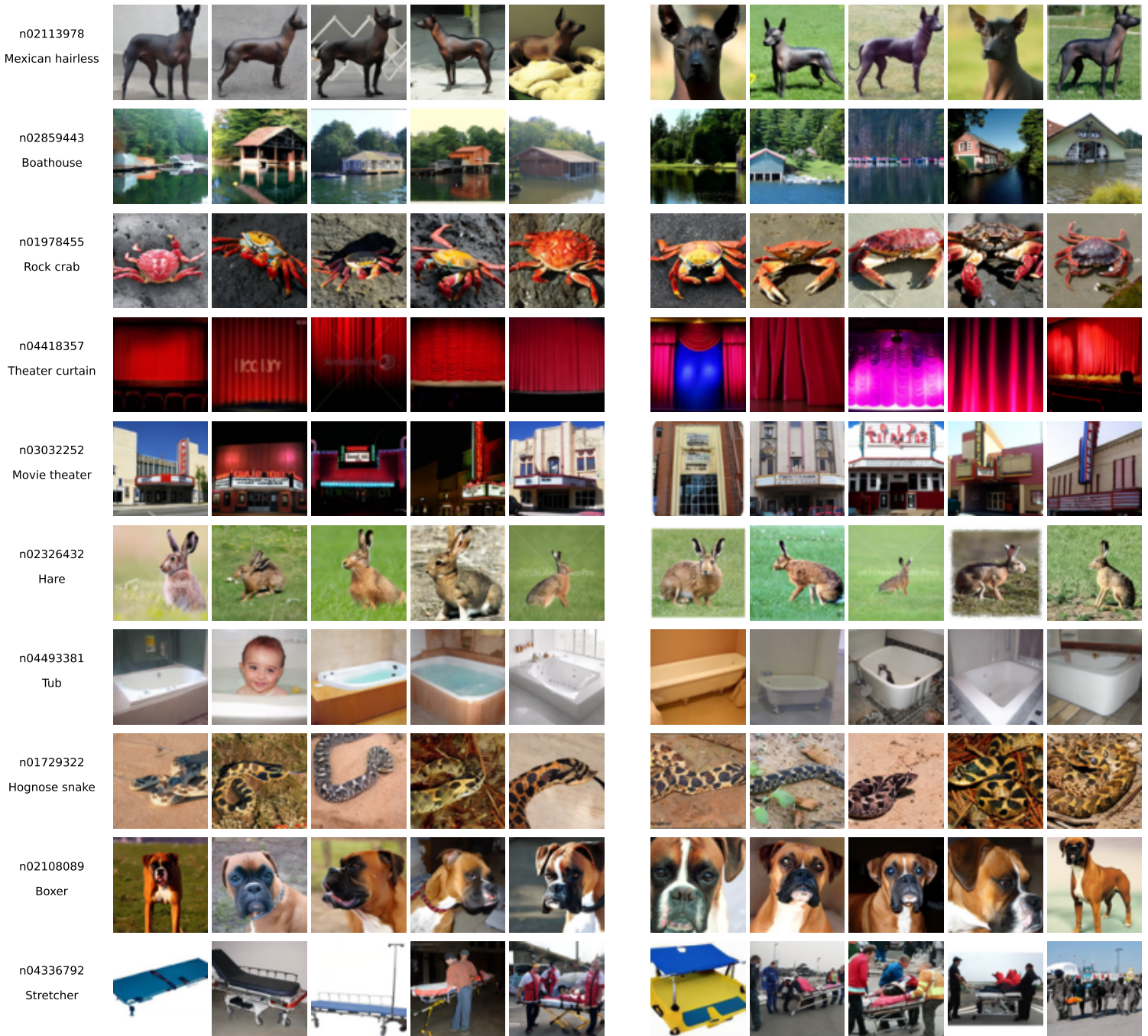


Figure 12. Comparison between samples selected by Minimax [8] (left) and generated by the proposed ImS^3 (right) for ImageNet-100 classes 10-19. The class names are marked at the left of each row.

MinimaxDiffusion

IMS³

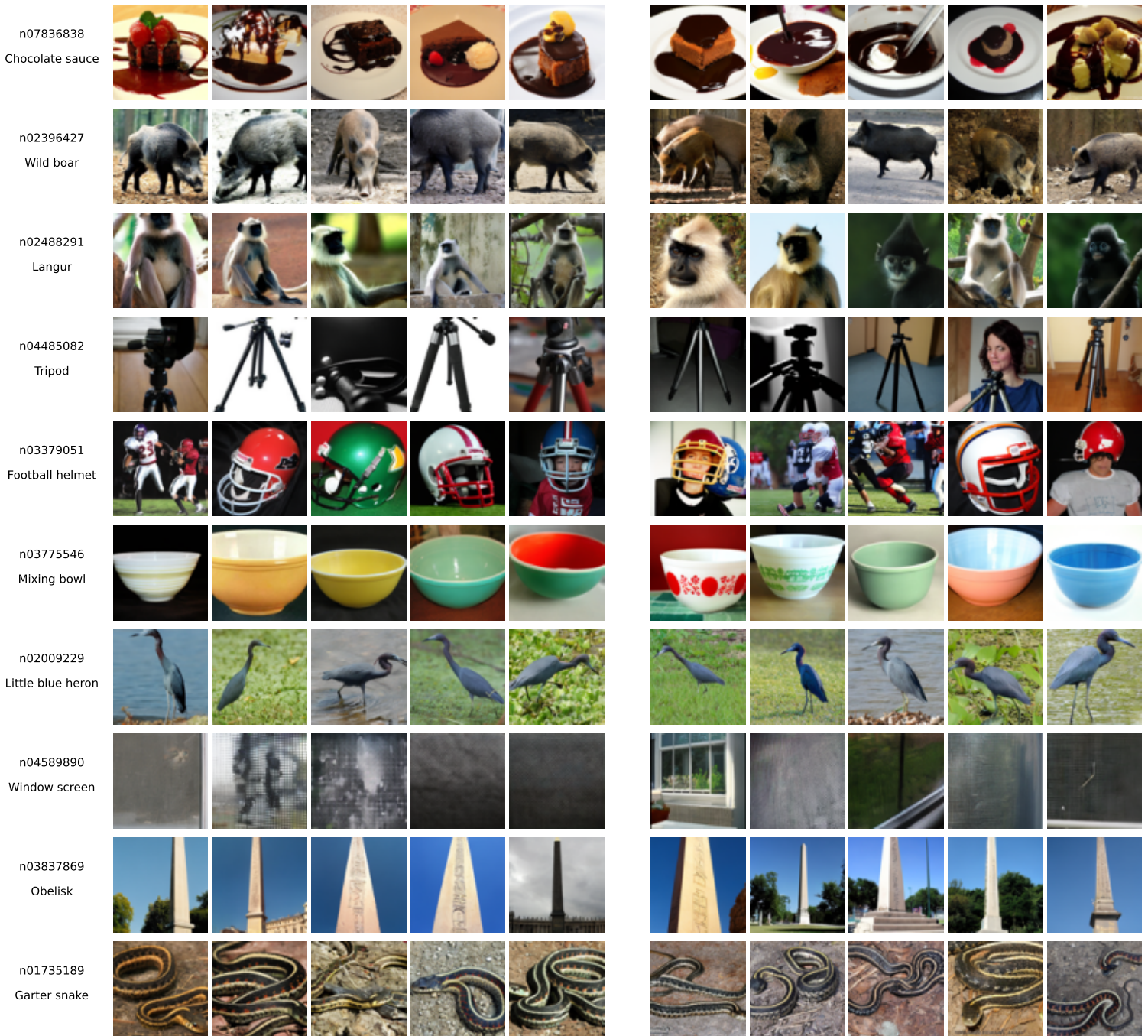


Figure 13. Comparison between samples selected by Minimax [8] (left) and generated by the proposed ImS³ (right) for ImageNet-100 classes 20-29. The class names are marked at the left of each row.

MinimaxDiffusion

IMS³

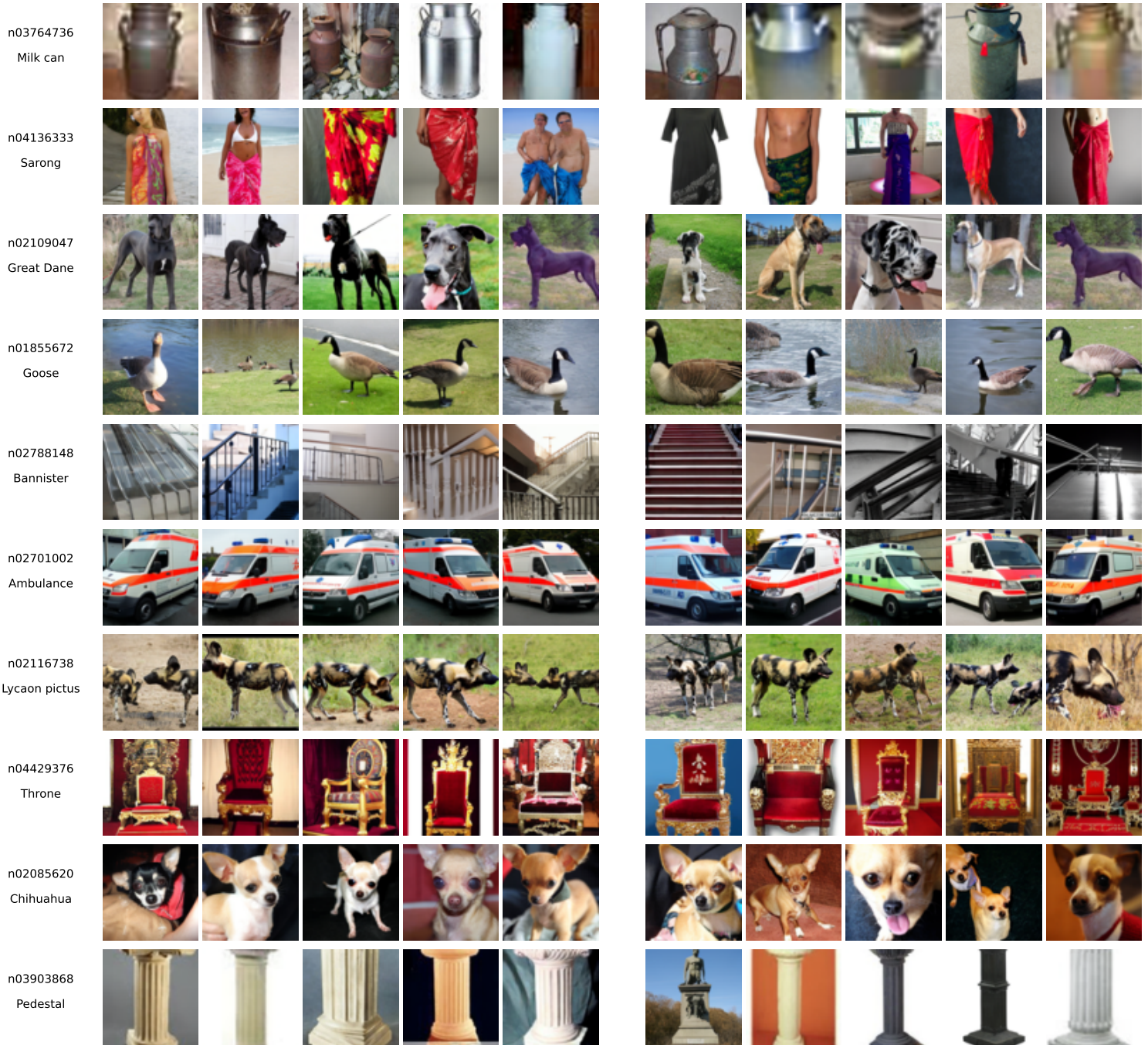


Figure 14. Comparison between samples selected by Minimax [8] (left) and generated by the proposed ImS³ (right) for ImageNet-100 classes 30-39. The class names are marked at the left of each row.

MinimaxDiffusion

IMS³

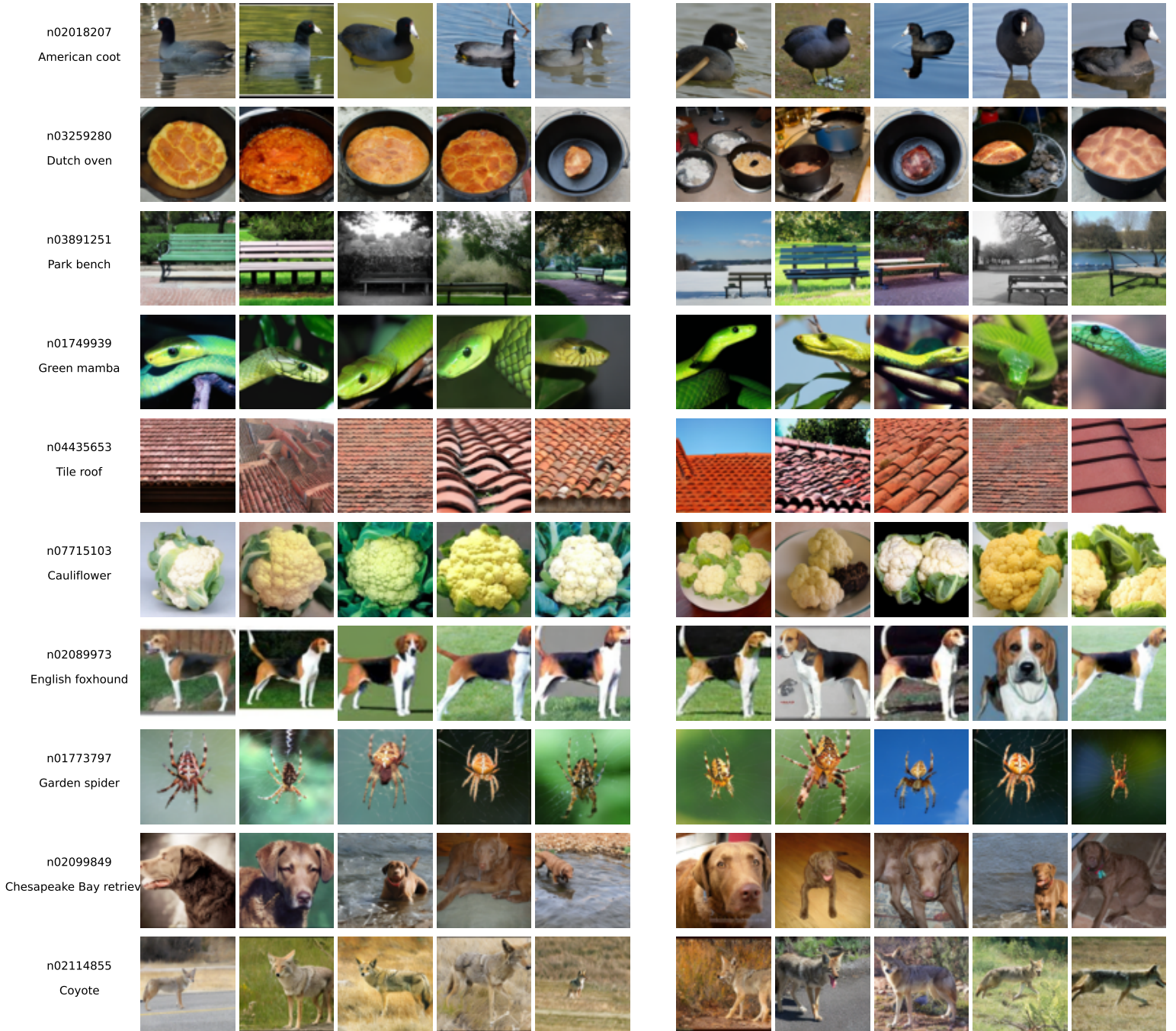


Figure 15. Comparison between samples selected by Minimax [8] (left) and generated by the proposed ImS^3 (right) for ImageNet-100 classes 40-49. The class names are marked at the left of each row.

MinimaxDiffusion

IMS³

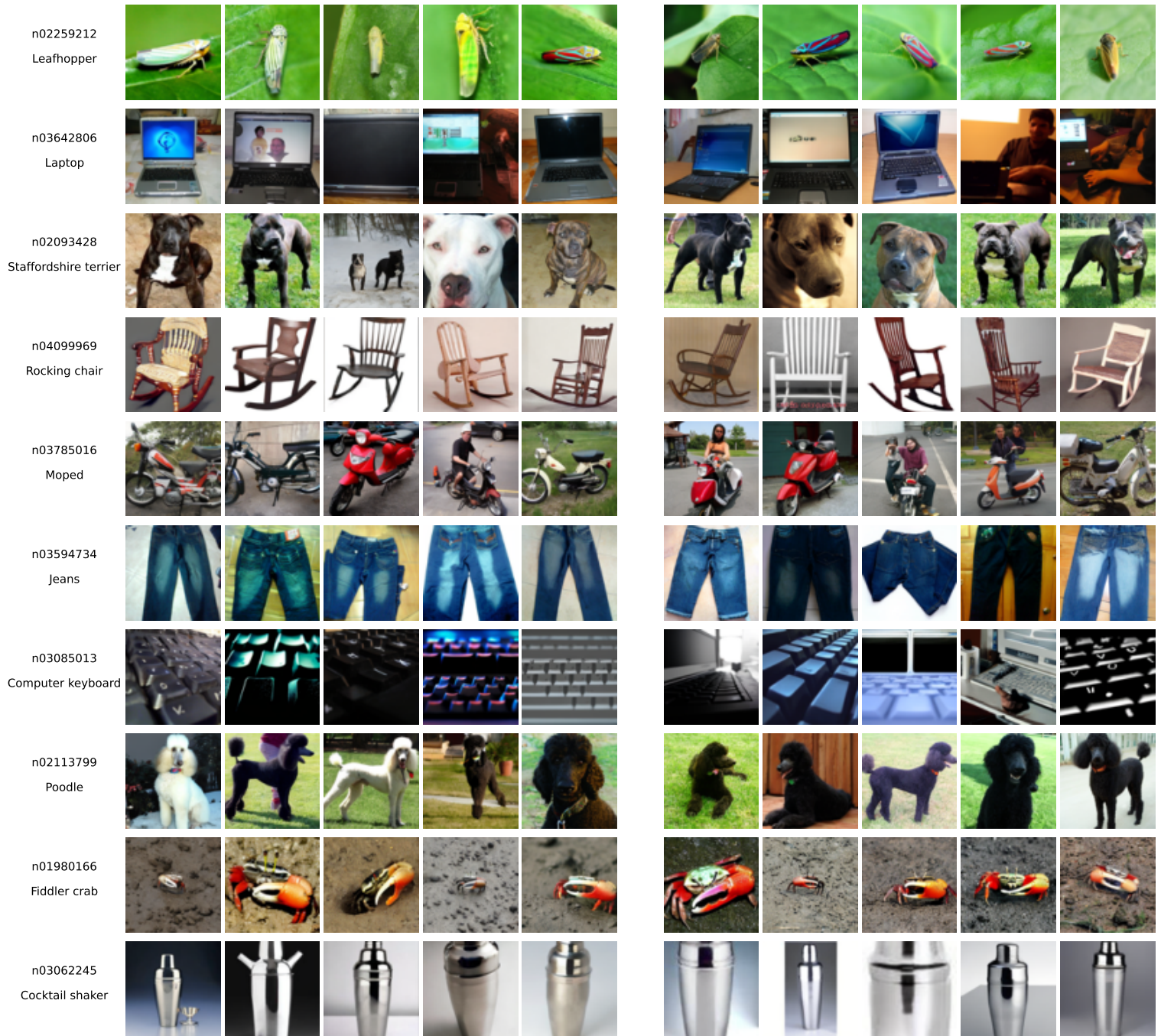


Figure 16. Comparison between samples selected by Minimax [8] (left) and generated by the proposed ImS³ (right) for ImageNet-100 classes 50-59. The class names are marked at the left of each row.

MinimaxDiffusion

IMS³

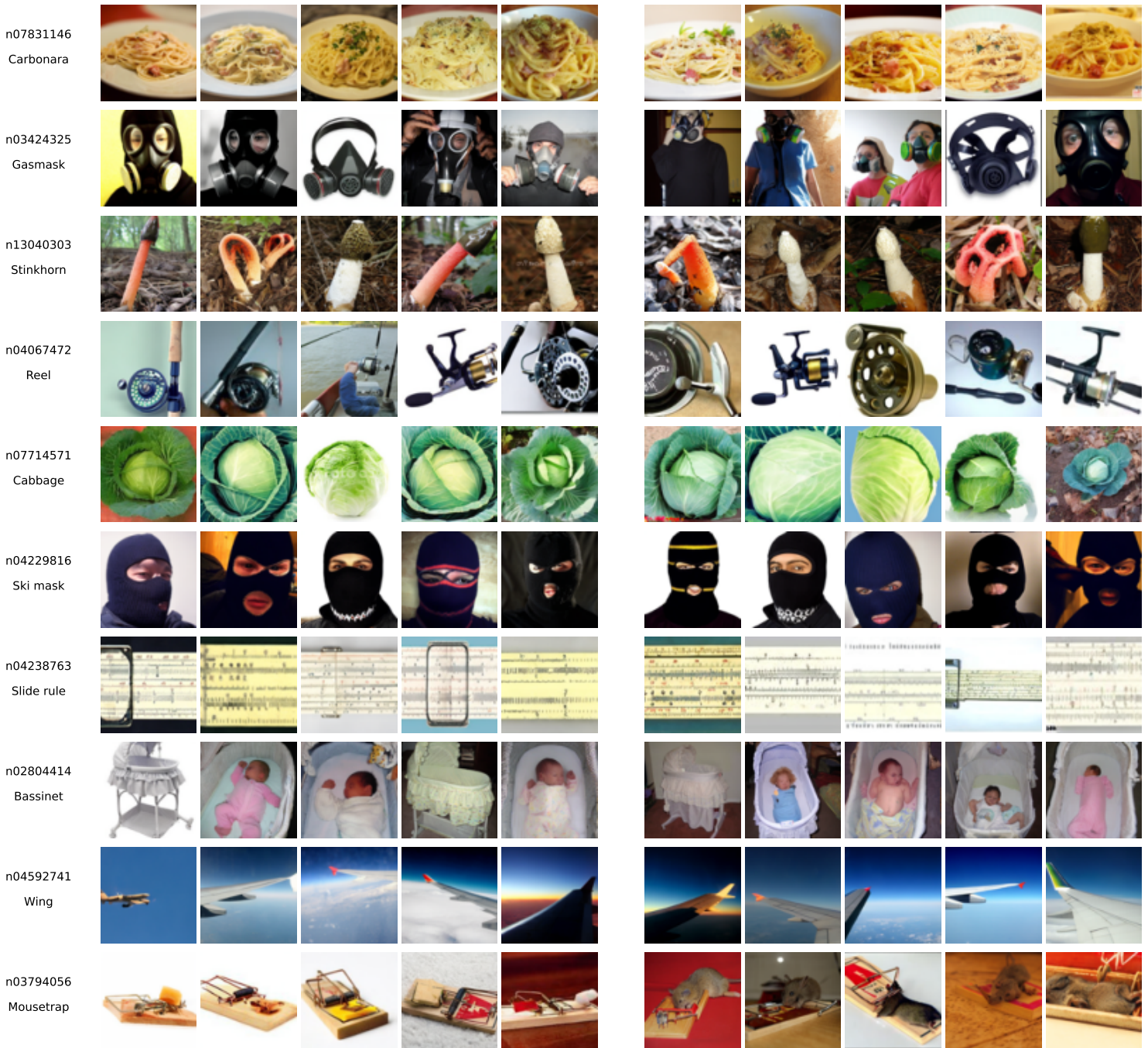


Figure 17. Comparison between samples selected by Minimax [8] (left) and generated by the proposed ImS^3 (right) for ImageNet-100 classes 60-69. The class names are marked at the left of each row.

MinimaxDiffusion

IMS³

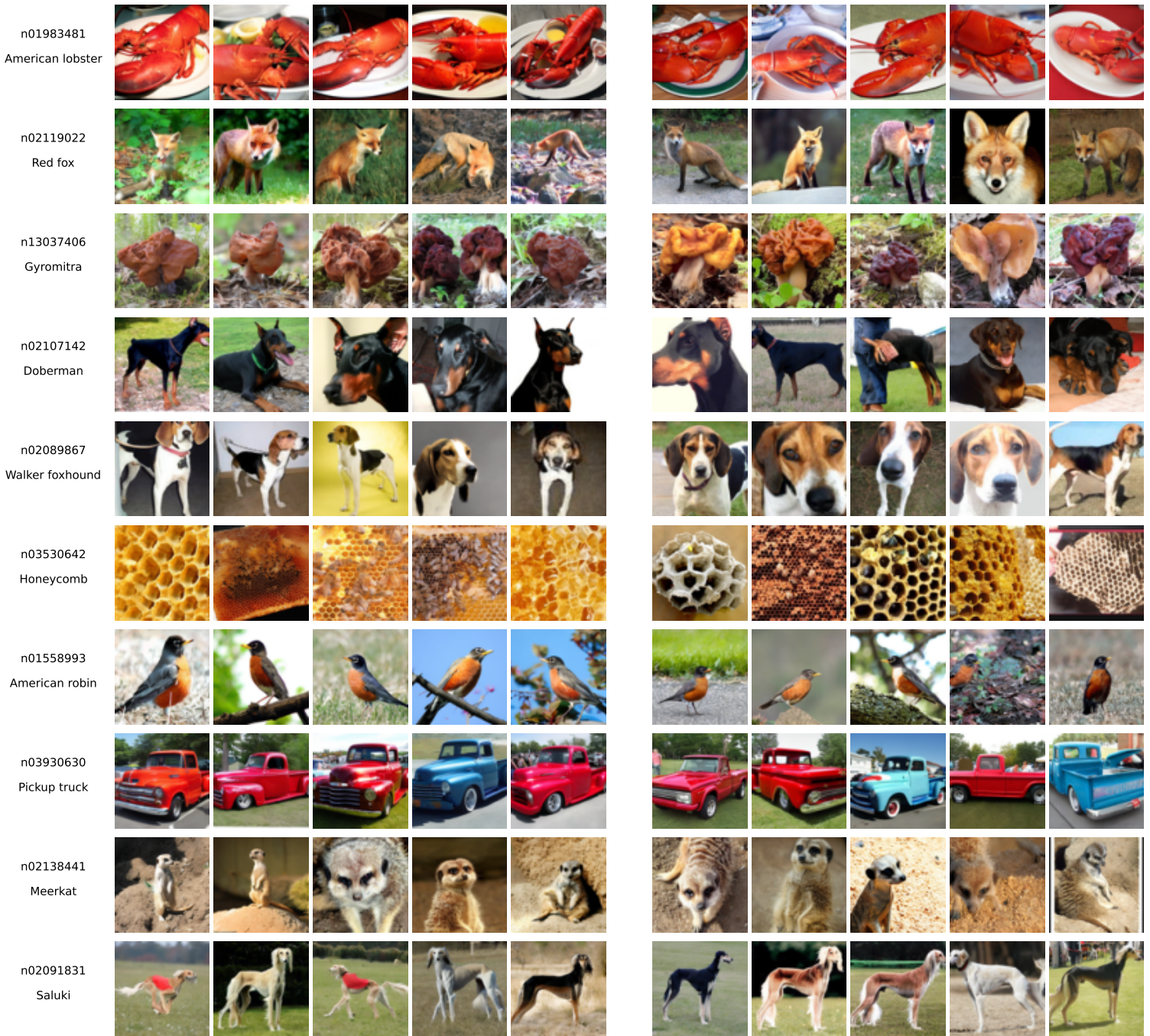


Figure 18. Comparison between samples selected by Minimax [8] (left) and generated by the proposed ImS^3 (right) for ImageNet-100 classes 70-79. The class names are marked at the left of each row.

MinimaxDiffusion

IMS³

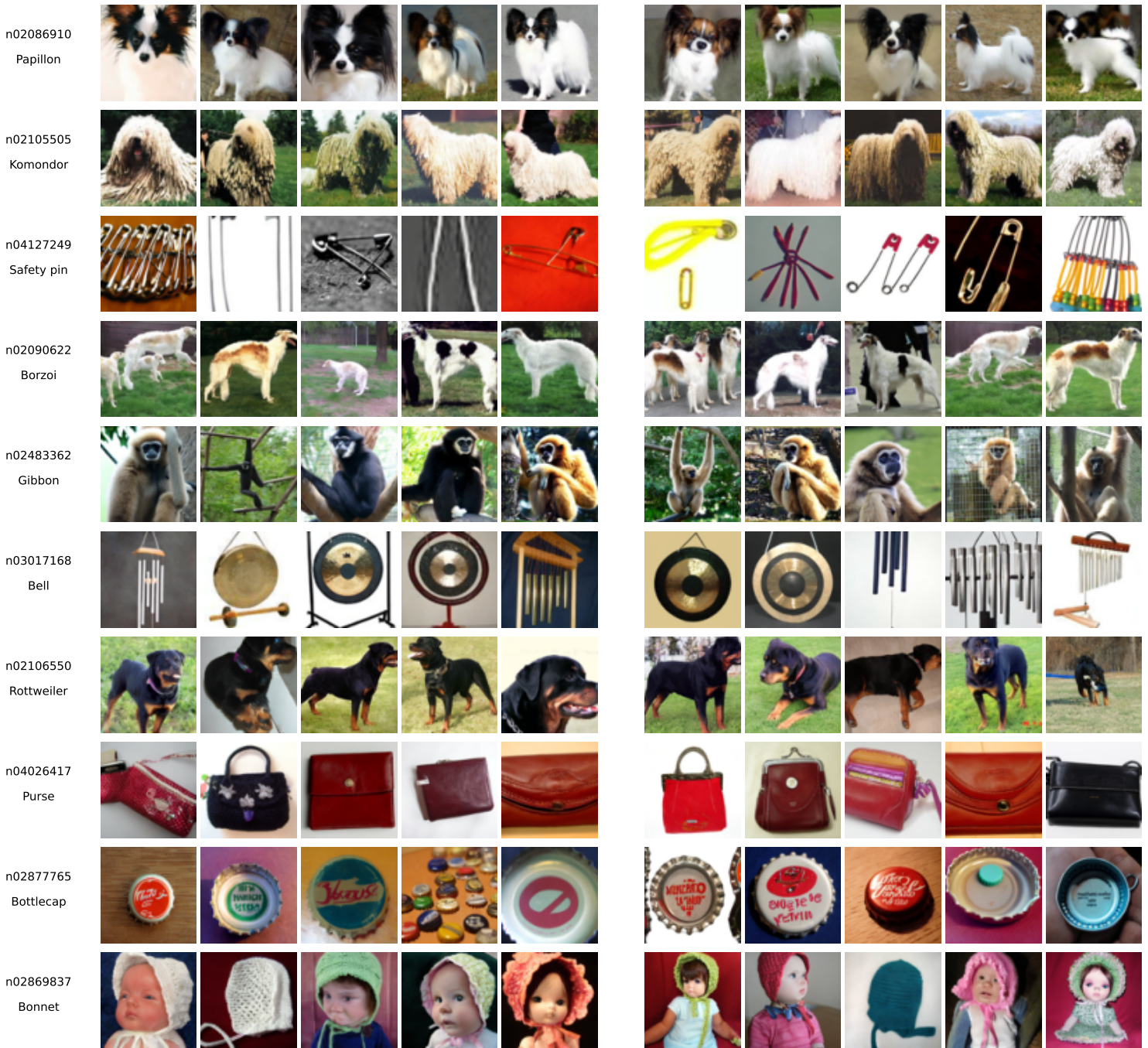


Figure 19. Comparison between samples selected by Minimax [8] (left) and generated by the proposed ImS³ (right) for ImageNet-100 classes 80-89. The class names are marked at the left of each row.

MinimaxDiffusion

IMS³

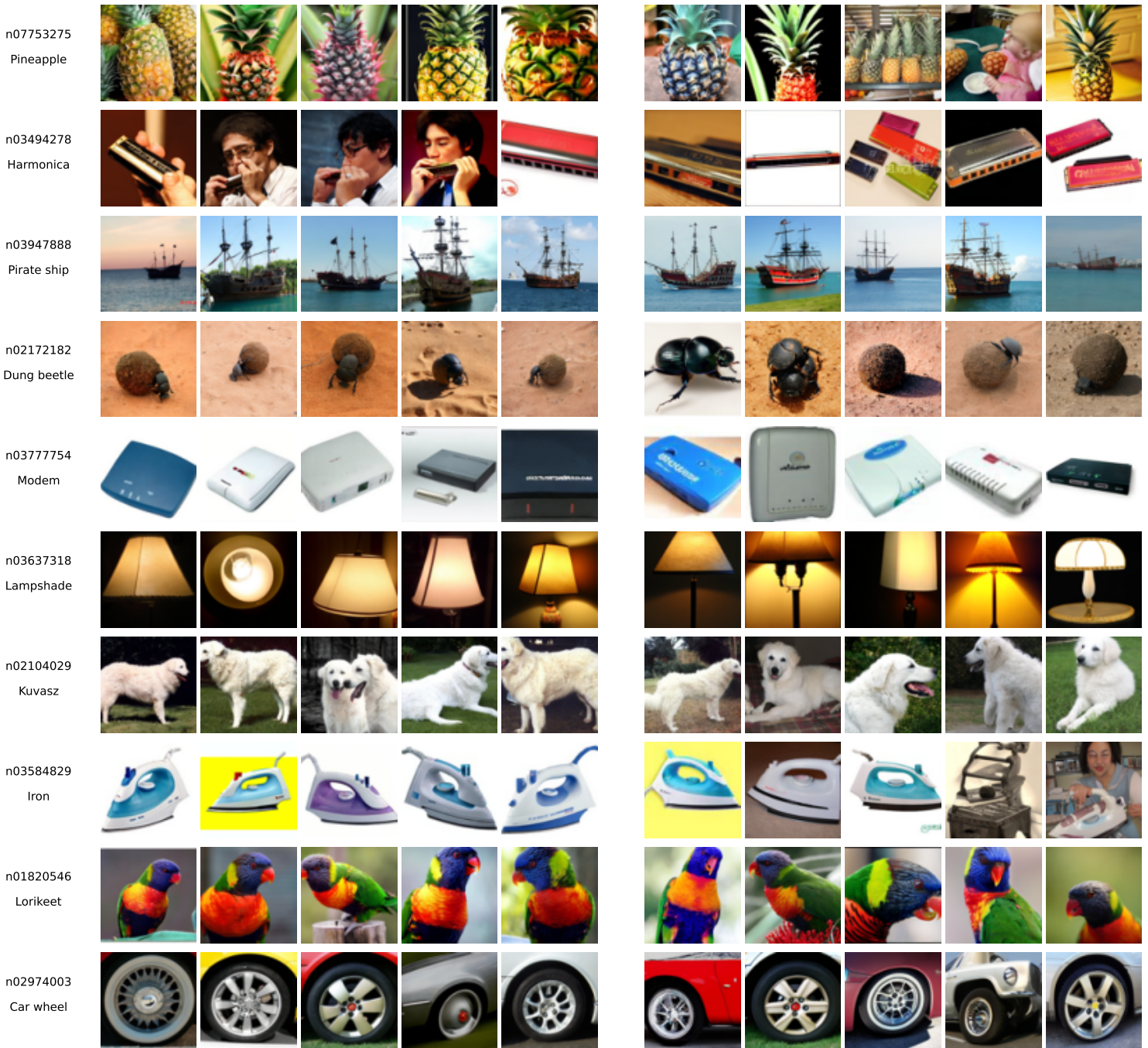


Figure 20. Comparison between samples selected by Minimax [8] (left) and generated by the proposed ImS^3 (right) for ImageNet-100 classes 90-99. The class names are marked at the left of each row.